ARTICLES

nature cell biology

iPSC-derived cardiomyocytes reveal abnormal TGF-β signalling in left ventricular non-compaction cardiomyopathy

Kazuki Kodo[1,2,7], Sang-Ging Ong[1,2,7], Fereshteh Jahanbani[3], Vittavat Termglinchan[1,2,4], Keiichi Hirono[5], Kolsoum InanlooRahatloo[1,2], Antje D. Ebert[1,2,4], Praveen Shukla[1,2], Oscar J. Abilez[1,2], Jared M. Churko[1,2,4], Ioannis Karakikes[1,2,4], Gwanghyun Jung[1,6], Fukiko Ichida[5], Sean M. Wu[1,2], Michael P. Snyder[3], Daniel Bernstein[1,6,8] and Joseph C. Wu[1,2,4,8]

Left ventricular non-compaction (LVNC) is the third most prevalent cardiomyopathy in children and its pathogenesis has been associated with the developmental defect of the embryonic myocardium. We show that patient-specific induced pluripotent stem cell-derived cardiomyocytes (iPSC-CMs) generated from LVNC patients carrying a mutation in the cardiac transcription factor TBX20 recapitulate a key aspect of the pathological phenotype at the single-cell level and this was associated with perturbed transforming growth factor beta (TGF-β) signalling. LVNC iPSC-CMs have decreased proliferative capacity due to abnormal activation of TGF-β signalling. TBX20 regulates the expression of TGF-β signalling modifiers including one known to be a genetic cause of LVNC, PRDM16, and genome editing of PRDM16 caused proliferation defects in iPSC-CMs. Inhibition of TGF-β signalling and genome correction of the TBX20 mutation were sufficient to reverse the disease phenotype. Our study demonstrates that iPSC-CMs are a useful tool for the exploration of pathological mechanisms underlying poorly understood cardiomyopathies including LVNC.

Left ventricular non-compaction (LVNC) is increasingly recognized as a cause of cardiomyopathy[1,2], especially in children. In a recent study, LVNC accounted for 9.2% of all children with primary cardiomyopathies, and was the third most prevalent form of cardiomyopathy, after dilated cardiomyopathy (DCM) and hypertrophic cardiomyopathy[2]. LVNC is characterized by deep and extensive hypertrabeculation of the left ventricle, and causes heart failure, arrhythmias and thromboembolism.

LVNC has been theorized to result from the arrest of compaction of the developing LV myocardium, as it passes through several distinct evolutionarily conserved steps. Trabeculations in the human embryo emerge after looping of the primitive heart tube at the end of the fourth week of gestation[3]. Trabecular remodelling begins at 8 weeks with an increase in LV volume compressing the trabeculations, leading to an increase in the thickness of the compacted myocardium. Serial pathologic studies suggest that LVNC arises from impaired/arrested compaction of the myocardium, or abnormalities of vascularization, or in development of the multilayered spiral system[3,4]. Among these steps, emergence of trabeculations and trabecular remodelling are thought to be the key steps to understanding LVNC. The trabeculation patterns are ventricle-specific, which are generally thicker and the corresponding intertrabecular spaces are larger in the LV than in the right ventricle. When this embryonic pattern persists postnatally, the morphologic appearance strongly resembles the embryonic 'spongiform' myocardium, which was the original nomenclature for this cardiomyopathy.

Like many congenital cardiomyopathies, the genetics of LVNC is complex and the full spectrum of the disorder is still undefined. The mechanisms that lead to LVNC are not well understood, although animal models of LVNC have suggested that abnormal regulation of growth signals, including the transforming growth factor beta (TGF-β)[5–9], NOTCH and NRG1/ERBB2[10,11], may be causative factors. Since most of these animal models harbouring non-compaction-like myocardium showed alterations in cell-cycle regulation in developing

[1]Stanford Cardiovascular Institute, Stanford University School of Medicine, Stanford, California 94305, USA. [2]Department of Medicine, Division of Cardiology, Stanford University School of Medicine, Stanford, California 94305, USA. [3]Department of Genetics, Stanford University School of Medicine, Stanford, California 94305, USA. [4]Institute of Stem Cell Biology and Regenerative Medicine, Stanford University School of Medicine, Stanford, California 94305, USA. [5]Department of Pediatrics, University of Toyama, Toyama-shi, Toyama 930-8555, Japan. [6]Department of Pediatrics, Stanford University School of Medicine, Stanford, California 94305, USA. [7]These authors contributed equally to this work.
[8]Correspondence should be addressed to D.B. or J.C.W. (e-mail: danb@stanford.edu or joewu@stanford.edu)

Received 3 September 2015; accepted 12 August 2016; published online 19 September 2016; DOI: 10.1038/ncb3411

cardiomyocytes, it is thought that the abnormal proliferation of embryonic cardiomyocytes may be associated with the pathogenesis of LVNC. However, studies have differed on whether this proliferation is increased or decreased[5–7,9]. Furthermore, recent human studies have identified mutations in genes that are associated with regulation of cardiomyocyte proliferation[11,12]. However, it is still unclear which phenotypes in developing cardiomyocytes are actually associated with the pathogenesis seen in humans and investigation of this disease has been challenging due to its complex genetic basis.

To overcome the problems for the investigation of human cardiac cell development with a pathological background of LVNC, we used patient-specific induced pluripotent stem cells (iPSCs). Here we demonstrated the use of human iPSC-derived cardiomyocytes (iPSC-CMs) from patients carrying the TBX20 mutation affected by LVNC as a model to define cell-specific phenotypes and elucidate potential mechanisms of this disease.

RESULTS

TBX20 mutation is a candidate genetic cause of LVNC

To identify potential genetic causes of LVNC, we recruited a family with LVNC including the proband no. 1 (A-III-4), who had undergone heart transplantation for restrictive physiology, two siblings (A-III-2 and A-III-3) with significantly deeper and more extensive trabeculation of the left ventricle (a forme fruste of LVNC referred to clinically as 'hypertrabeculation') but with normal systolic function, and the father (A-II-2) with asymptomatic DCM without LVNC (Fig. 1a–c and Supplementary Table 1). Genetic testing by genome-wide exome sequencing revealed a stop-gain mutation in the TBX20 gene (Y317*) in the proband no. 1, two siblings, and father (Fig. 1d). No mutations in maternally transmitted and *de novo* modifiers known to contribute to cardiomyopathies were detected (Supplementary Table 2). To investigate whether TBX20 mutations are seen in other LVNC patients, we performed genetic testing in an additional 77 LVNC patients and detected another *de novo* mutation (T262M) from one additional isolated LVNC patient (proband no. 2: B-II-2) (Fig. 1a,b,d and Supplementary Table 1).

TBX20 is an essential cardiac transcription factor that regulates cardiomyocyte differentiation and proliferation[13,14]. TBX20 has also been described in conjunction with congenital heart disease[15–17] and DCM[18,19]. The TBX20 Y317* mutation resulted in a truncated protein (Fig. 1e). TBX20 Y317* and T262M mutant proteins showed disturbed synergistic activity with other cardiac transcription factors, including NKX2-5, GATA4 and TBX5 (Supplementary Fig. 1a,b). Furthermore, both TBX20 Y317* and T262M mutations were found to impair the negative transcriptional regulatory function of TBX20 compared with the wild type (Supplementary Fig. 1c). These results suggest that LVNC-associated mutations caused disturbance of transcriptional regulation by TBX20.

LVNC iPSC-CMs possess a defect of proliferative capacity

To investigate the pathological mechanism of LVNC, we generated iPSCs using Sendai virus reprogramming from a family with an LVNC history along with three unrelated control volunteers[20,21]; two clones per patient were established (Supplementary Fig. 1d–f and Supplementary Table 3). We classed all lines into three subgroups: unrelated control, mild DCM (A-II-2) and LVNC (A-III-2, 3, 4). iPSCs were differentiated into cardiomyocytes (iPSC-CMs)[22], followed by glucose deprivation to enrich for iPSC-CMs (Supplementary Fig. 2a)[23]. Although LVNC iPSC-CMs were similar to control iPSC-CMs in terms of structural and electrophysiological phenotype as well as sarcomeric gene expression at 2–4 weeks, LVNC iPSC-CMs showed an approximately 50% reduction of the expression of TBX20 downstream target genes compared with control iPSC-CMs (Fig. 1f and Supplementary Fig. 2b–j and Supplementary Table 4). Furthermore, the differentiation efficiency was also halved in LVNC iPSC lines compared with the control prior to glucose deprivation (Fig. 1g). On the other hand, mild DCM iPSC-CMs showed intermediate defects in TBX20 target gene expression and differentiation efficiency between LVNC and control iPSC-CMs. Despite comparable expression of mesodermal markers including MESP1 and brachyury (T) across all lines during cardiac differentiation (Supplementary Fig. 2k), LVNC iPSCs had significantly lower expression of cardiac transcription factors compared with control cell lines especially between day 6 and 9 (Fig. 1h and Supplementary Fig. 3a). These results suggest an impaired induction of cardiac lineage from mesodermal progenitors in LVNC iPSCs.

Since past human and mouse studies have shown possible association between cell-cycle defects in developing cardiomyocytes and pathogenesis of LVNC[5–7,12,24], we next assessed the proliferative potential in iPSC-CMs. We found that iPSC-CMs were responsive to growth factors and had increased numbers within 3 weeks after induction of differentiation although their growth was temporary (Supplementary Fig. 3b). To assess the proliferation potential in developing iPSC-CMs, the distribution of S-phase cardiomyocytes was validated by EdU incorporation with or without stimulation of serum or growth factors. LVNC iPSC-CMs showed reduced baseline proliferative capacity by ∼50% without any stimulation as well as in the presence of serum and growth factors compared with control cells at an earlier time point (2 weeks), whereas mild DCM iPSC-CMs showed a milder reduction of ∼30% compared with control (Fig. 1i,j). On the other hand, undifferentiated iPSCs showed no significant difference in their growth speed (Supplementary Fig. 3c), suggesting that the proliferation defect may be characteristic in differentiated cardiac cells.

Abnormal activation of TGF-β signalling is associated with proliferation defect in LVNC iPSC-CMs

To clarify potential signalling pathways associated with the proliferation defect in LVNC iPSC-CMs, we next performed RNA-sequencing using control, mild DCM, and LVNC iPSC-CMs at 2 weeks. Upstream regulator analysis predicted that activation of TGF-β signalling may be potentially responsible for this differential gene expression between control and LVNC iPSC-CMs (Fig. 2a and Supplementary Fig. 4a and Supplementary Table 5). Most of the TGF-β signalling pathway, especially TGF-β1-associated genes, were upregulated in LVNC and mild DCM iPSC-CMs compared with control iPSC-CMs (Fig. 2b and Supplementary Fig. 4b,c). Previous studies have shown that aberrant TGF-β signalling causes incomplete compaction of myocardium in mice[6,9], and that TGF-β signalling inhibits proliferation of embryonic cardiomyocytes[25,26] via upregulation of cyclin-dependent kinase inhibitors (CKIs) including CDKN1A[27–29]. Consistent with these studies, LVNC iPSC-CMs showed significant upregulation of TGF-β signalling-related genes and 1.7-fold higher phosphorylation of SMAD2/3 (Fig. 2c and

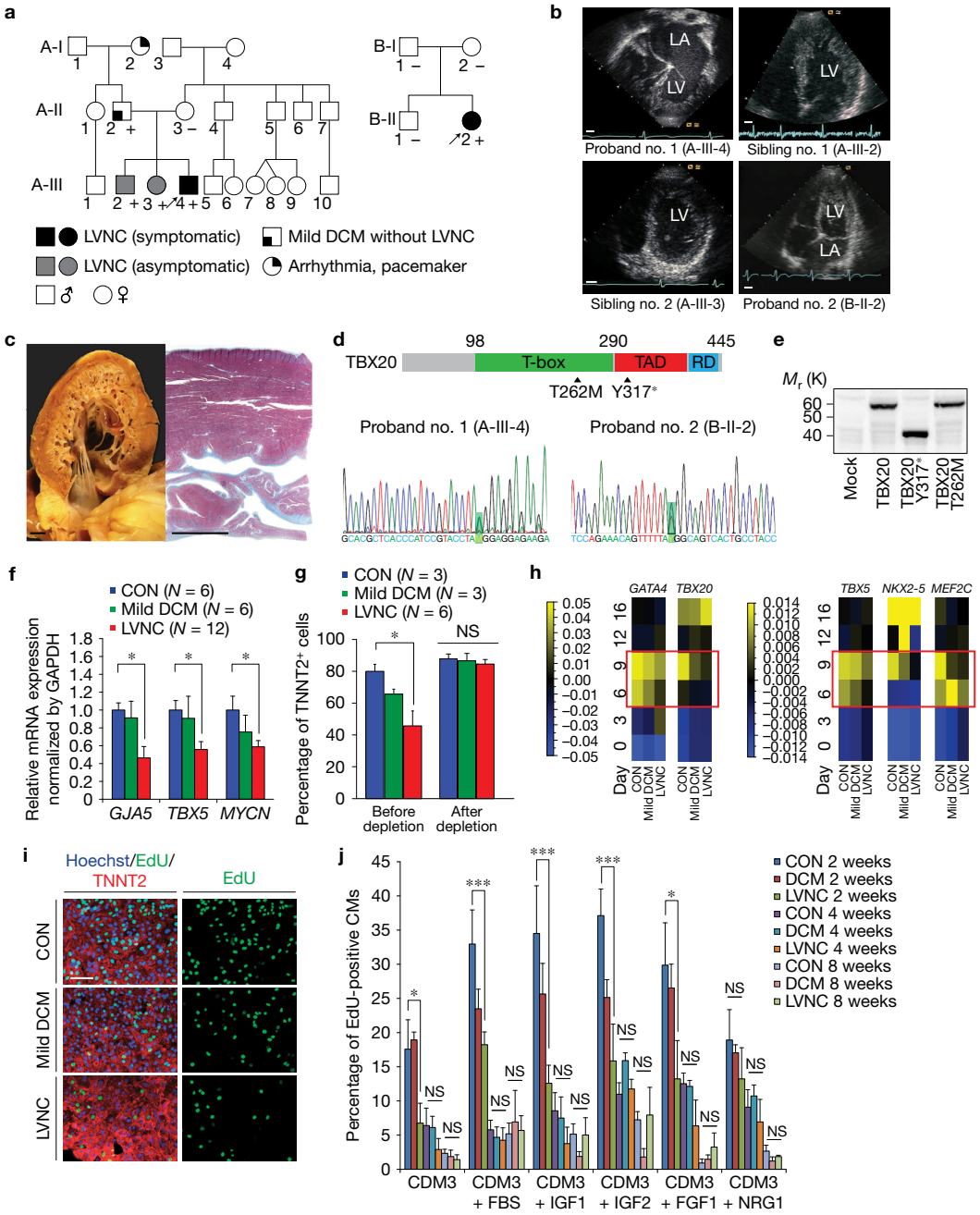

Figure 1 Characterization of patient-specific LVNC iPSC-CMs carrying a TBX20 mutation. (**a**) Schematic pedigree of two families with LVNC. The probands are indicated by arrows (A-III-4 and B-II-2). Plus and minus signs indicate the presence and absence of the TBX20 Y317* mutation in the family A and the T262M mutation in the family B, respectively. (**b**) The LVNC phenotype of the proband no. 1 (A-III-4), two siblings (A-III-2 and A-III-3), and an isolated proband no. 2 (B-II-2) is assessed by echocardiography. LA, left atrium; LV, left ventricle. Scale bars, 1 cm. (**c**) The proband no. 1's explanted heart (left) and Masson's trichrome staining of the left ventricle (right). Scale bars, 1 cm. (**d**) Schema of TBX20 and the position of the Y317* and T262M mutations (upper). Confirmation of the Y317* (c. 951C>A) and T262M (c. 785C>T) mutation on the *TBX20* gene (highlighted in green) (lower). TAD, transactivation domain; RD repression domain. (**e**) Western blot of FLAG-tagged wild-type, Y317* and T262M TBX20 mutant protein overexpressed in HEK293 cells. (**f**) Significant downregulation of *TBX20* downstream target gene mRNA expression in LVNC iPSC-CMs. (**g**) The efficiency of cardiac differentiation of patient-specific iPSC lines validated by FACS sorting. (**h**) Heat map showing mRNA expression of cardiac transcription factors in iPSCs from day 0 to day 16 after induction of cardiac differentiation. The LVNC iPSCs showed a significant decrease in cardiac transcription factors in day 6 and day 9 (red boxes). $n = 6$ independent experiments. Mean = 0. (**i**) Immunostaining of nuclear (blue), TNNT2 (red) and EdU (green) in iPSC-CMs at 2 weeks. Scale bar, 100 μm. (**j**) Percentage of EdU$^+$ cardiomyocytes in control, mild DCM, and LVNC iPSC-CMs with or without serum (FBS; $n = 10$, 10 and 30 for CON, mild DCM and LVNC independent experiments respectively at 2 weeks; $n = 4$ independent experiments per group at 4 and 8 weeks) or with growth factors (IGF1, IGF2, FGF1 or NRG1; $n = 4$ independent experiments per group at 2, 4 and 8 weeks). CON, unrelated controls. $^*P < 0.05$, $^{***}P < 0.005$; NS, not significant in one-way ANOVA followed by Tukey *post hoc* test. The bar graphs show the mean and error bars represent s.e.m. Statistics source data can be found in Supplementary Table 12. Unprocessed original scans of blots are shown in Supplementary Fig. 8.

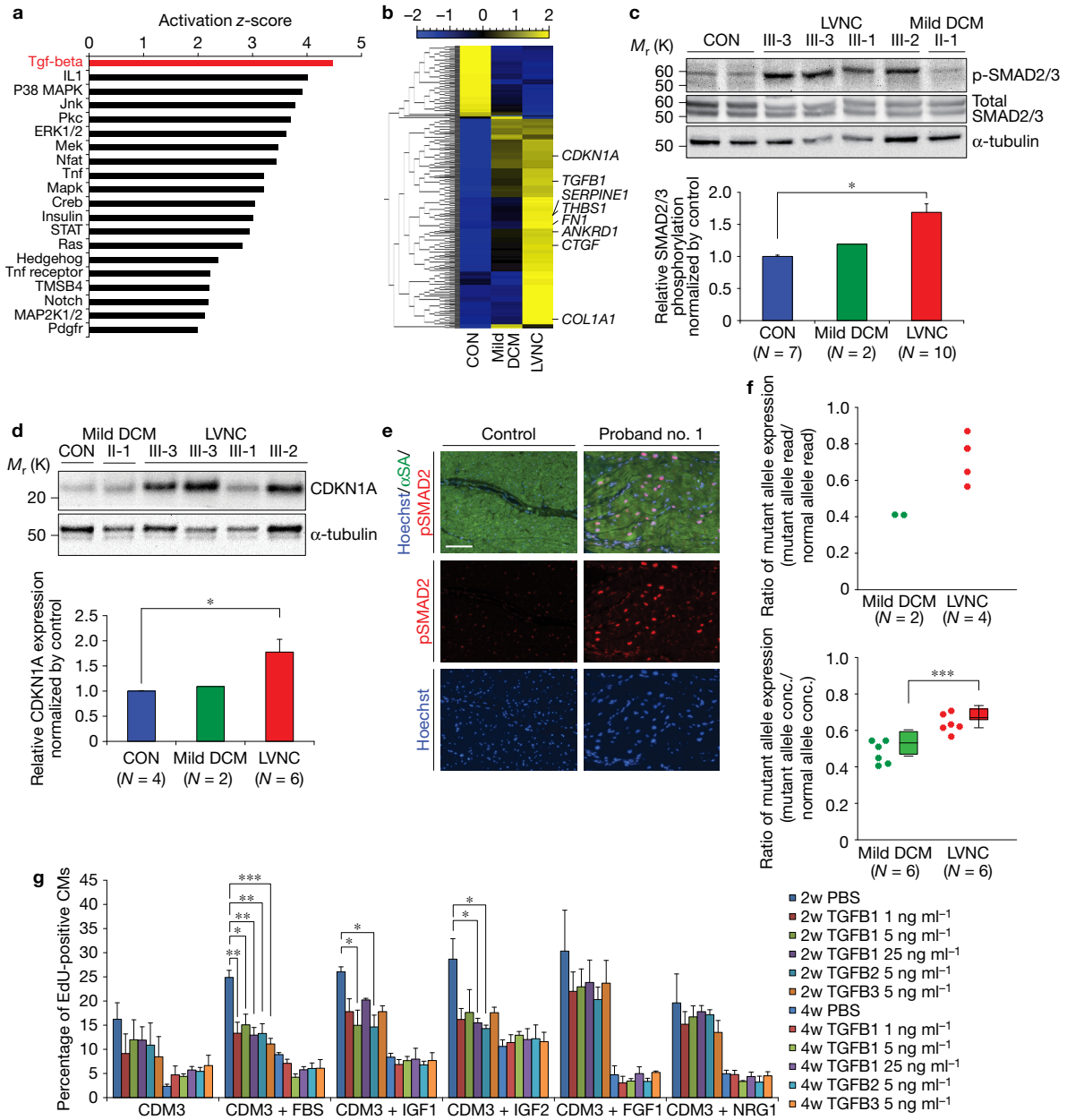

Figure 2 Upregulation of TGF-β signalling in the LVNC phenotype. (**a**) Upstream regulator analysis of the signalling pathway comparing LVNC and control iPSC-CMs at 2 weeks after induction of cardiac differentiation. (**b**) Heat map showing upregulation of the TGF-β signalling pathway in LVNC (III-2, 3, 4; mean of four samples) and mild DCM (II-2; mean of two samples) compared with control iPSC-CMs (unrelated controls; mean of two samples). Mean = 0, variance = 1. (**c**) Western blot of total and phospho-SMAD2/3 in control and patient-specific iPSC-CMs (upper) and densitometry analysis, normalized against α-tubulin (lower). (**d**) Western blot of CDKN1A protein in control and patient-specific iPSC-CMs (upper) and densitometry analysis, normalized against α-tubulin (lower). (**e**) Immunostaining of nuclear (blue), alpha-sarcomeric actin (green) and phospho-SMAD2 (red) in the LV of control donor heart tissue versus the explanted heart of proband no. 1. (**f**) Allele-specific mRNA expression analysis by mRNA-sequencing (upper panel) and digital droplet PCR (lower panel) showed a higher ratio of *TBX20* mutant allele expression in LVNC iPSC-CMs compared with mild DCM iPSC-CMs. $n = 6$ independent experiments. (**g**) The effect of TGF-β isoform treatments on the percentage of EdU$^+$ cardiomyocytes in control iPSC-CMs with or without growth factors. PBS-treated control; $n = 4$ independent experiments, TGF-β-treated samples; $n = 3$ independent experiments. CON, unrelated controls. $^*P < 0.05$, $^{**}P < 0.01$, $^{***}P < 0.005$ in unpaired two-tailed *t*-test or one-way ANOVA followed by Tukey *post hoc* test. The bar graphs show the mean and error bars represent s.e.m. Scale bar, 100 μm. Statistics source data can be found in Supplementary Table 12. Unprocessed original scans of blots are shown in Supplementary Fig. 8.

Supplementary Fig. 4d,e), whereas mild DCM iPSC-CMs had less phosphorylation (1.2-fold versus control). LVNC iPSC-CMs also showed a 1.8-fold increased CDKN1A expression compared with control iPSC-CMs (Fig. 2d and Supplementary Fig. 4f,g), suggesting that activation of the TGF-β1-CDKN1A regulatory axis may be responsible for the early cell-cycle exit seen in LVNC iPSC-CMs. Histological analysis of the proband's explanted LV myocardium revealed higher phosphorylation of SMAD2 in comparison with

control LV tissue, providing further evidence of activated TGF-β signalling as a pathogenesis of LVNC (Fig. 2e). Interestingly, LVNC iPSC-CMs showed significantly higher expression of TGF-β signalling pathway-associated genes compared with mild DCM iPSC-CMs that were associated with milder phenotypic severity (Supplementary Fig. 4b–g).

To understand the difference in disease severity between the father (mild DCM phenotype) and his children (LVNC phenotype), despite carrying the same TBX20 mutation, we next assessed expression of the mutant TBX20 allele by RNA-sequencing and digital droplet PCR. We found that the ratio of mutant allele against wild-type allele expression was higher in LVNC iPSC-CMs than in mild DCM iPSC-CMs (Fig. 2f), suggesting a dosage effect of the TBX20 mutant allele on the ectopic activation level of the TGF-β signalling pathway in patient-specific iPSC-CMs and perhaps explaining the differences in phenotypic severity among affected family members. To confirm that stimulation with TGF-β isoforms could affect the proliferation potential in iPSC-CMs, we treated control iPSC-CMs with TGF-β isoforms with or without serum or growth factors. We found that, like LVNC iPSC-CMs, TGF-β-treated control iPSC-CMs showed a significant decrease of proliferative response to serum, IGF-1, and IGF-2 stimulation at 2 weeks compared with TGF-β-untreated control iPSC-CMs (Fig. 2g). These results suggest that activation of TGF-β signalling has a negative effect on the proliferative potential of developing cardiomyocytes.

Ectopic activation of TGF-β signalling causes a cardiomyocyte proliferation defect *in vivo*

To assess how abnormal TGF-β1 signalling affects myocardial development *in vivo*, we next generated cardiac-specific TGF-β1-overexpressing transgenic mice ($\beta1^{glo}$/αMHC-Cre; Supplementary Fig. 5). These double-transgenic mice exhibit embryonic lethality by embryonic day (E) 11.5 due to decreased proliferation in developing cardiomyocytes (Fig. 3a–d and Supplementary Fig. 5c and d and Supplementary Table 6), providing further proof implicating aberrant TGF-β signalling in the embryonic heart with developmental arrest of the compact layer.

Next, to assess the later stages of compact layer development, we crossed $\beta1^{glo}$ transgenic mice with NK-TGCK transgenic mice that express GFP-Cre fusion protein under the control of the Nkx2-5 cardiac-specific enhancer/promoter and Tet-Off system to negatively regulate GFP-Cre expression following doxycycline (DOX) exposure (Supplementary Fig. 5e). The αMHC-Cre transgene labelled >90% of cardiomyocytes at E12.5 and the NK-TGCK transgene activated Cre in ∼40% of cardiomyocytes without DOX and ∼25% of cardiomyocytes with DOX treatment and showed significantly lesser TGFB1 mRNA expression compared with αMHC-Cre/$\beta1^{glo}$ double-transgenic mouse embryos at E10.5 (Supplementary Fig. 5f–h). The double-transgenic embryos carrying both NK-TGCK and $\beta1^{glo}$ ($\beta1^{glo}$/NK-TGCK) without DOX treatment showed a significant increase of TGF-β downstream target genes whereas the double-transgenic embryos with DOX treatment showed only a mild increase of these genes at E10.5 (Supplementary Fig. 5i). The $\beta1^{glo}$/NK-TGCK double-transgenic embryos showed embryonic lethality around E12.5 to E13.5. In contrast, when mice were treated with DOX, the embryos could survive normally at E12.5 (Fig. 3e and Supplementary Table 7). Histological analysis showed a significantly thinner compact layer and reduced Ki67 or phospho-histone H3 (PHH3)-positive cardiomyocytes in the compact layer in $\beta1^{glo}$/NK-TGCK double-transgenic embryos without DOX compared with wild-type littermates, although the trabecular layer was well developed in these double-transgenic embryos (Fig. 3f–h and Supplementary Fig. 5j,k). Half of DOX-treated $\beta1^{glo}$/NK-TGCK double-transgenic embryos showed reduced thickness of the LV compact layer, and the proportion of $Ki67^{+}$ or $PHH3^{+}$ cardiomyocytes in the compact layer in $\beta1^{glo}$/NK-TGCK embryos was mildly decreased compared with wild-type littermates (Fig. 3f,i,j and Supplementary Fig. 5j,k).

To assess the fate of TGF-β1-activated CMs in DOX-treated transgenic mice, we next generated triple-transgenic embryos carrying NK-TGCK/$\beta1^{glo}$ transgenes with a Cre-dependent tdTomato overexpression system (Ai14)[30]. We found that the proportion of TGF-β1-activated CMs in LV was significantly decreased in triple-transgenic embryos and neonates during development compared with control (NK-TGCK/Ai14) mice, suggesting reduced proliferation by TGF-β-expressing CMs (Fig. 4a,b). Furthermore, the hearts of triple-transgenic neonates at postnatal day 3 showed a thicker trabecular layer and a thinner compact layer resulting in a significantly higher non-compaction/compaction (NC/C) ratio in LV myocardium compared with control neonates (Fig. 4c–e). Taken together, these results support the role of abnormal activation of TGF-β signalling to cause developmental arrest of cardiomyocytes in a temporal and dose-dependent manner *in vivo*.

Functional disturbance of TBX20 causes abnormal activation of TGF-β signalling

Next, to assess whether the defective TBX20 transcriptional cascade causes abnormal activation of TGF-β signalling, we analysed the gene expression profile of the Tbx20 knockout mouse[31]. Interestingly, messenger RNA expression analysis of Tbx20 knockout mouse heart revealed a similar gene expression profile to that of LVNC iPSC-CMs, including upregulation of TGF-β signalling (Fig. 5a and Supplementary Table 8)[31]. Furthermore, ChIP-sequencing data of Tbx20[31] showed conserved TBX20-binding sites in the genes that are associated with TGF-β signalling regulation and modification between human and mouse (Fig. 5b and Supplementary Table 9). This gene expression profile was significantly disturbed in LVNC iPSC-CMs compared with control iPSC-CMs, as well as in the Tbx20 knockout mouse heart compared with the wild type (Fig. 5c,d). We further employed short hairpin RNA (shRNA) against TBX20 in the H7 human embryonic stem cell (ESC) line (TBX20KD-H7) (Fig. 6a,b), and found that TBX20KD-H7-CMs showed less proliferative capacity and increased expression of TGF-β-related genes compared with scramble control lines (Fig. 6c–g). These results confirm that the dysfunction of TBX20 is associated with the pathological proliferation phenotype of LVNC iPSC-CMs through disturbance of the TGF-β signalling.

TBX20–PRDM16 axis regulates TGF-β signalling and contributes to cardiomyocyte proliferation

To better understand the regulatory mechanism of TGF-β signalling by TBX20, we next studied TGF-β modifiers with conserved TBX20-binding sites[31] between human and mouse (Supplementary Table 9), and selected the PRDM16 gene as one of the potential

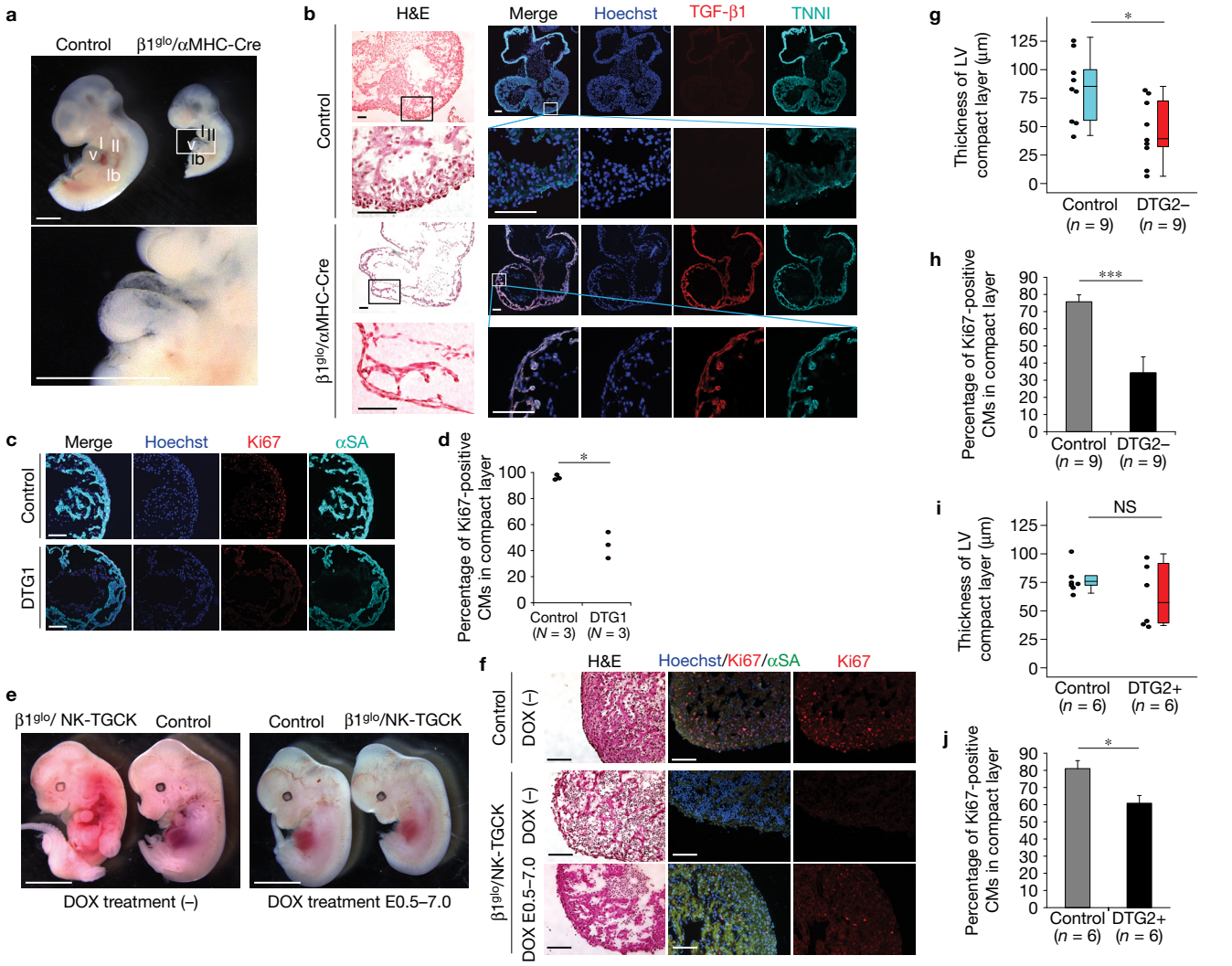

Figure 3 Developmental arrest in cardiomyocyte-specific TGF-β1-overexpressing mouse embryo heart. (**a**) Lateral view of a double-transgenic embryo ($\beta1^{glo}$/αMHC-Cre) at embryonic day (E) 10.5 compared with a wild-type littermate (control). The lower panel shows a higher-magnification view of the double-transgenic embryo heart (white box in upper panel). Scale bars, 1 mm. (**b**) Haematoxylin and eosin (H&E) staining and immunostaining of nuclear (blue), TGF-β1 (red) and TNNI (cyan) in control and $\beta1^{glo}$/αMHC-Cre double-transgenic (DTG1) embryo hearts at E10.5. Higher-magnification pictures of the compact layer (indicated by the white box in the upper panels) are shown in the lower lane. Scale bars, 100 μm. (**c**) Immunostaining for nuclear (blue), Ki67 (red) and αSA (cyan) in coronal sections of control and DTG1 hearts at E10.5. Scale bars, 100 μm. (**d**) Percentage of $Ki67^+$ cardiomyocytes in the compact layer of control and DTG1 embryo hearts at E10.5. (**e**) The systemic phenotypes of a partially TGF-β1-overexpressing double-transgenic embryo ($\beta1^{glo}$/NK-TGCK) at E12.5 compared with the wild-type littermate (control) with or without doxycycline (DOX) treatment. Scale bars, 5 mm. (**f**) H&E and immunostaining of nuclear (blue), Ki67 (red) and αSA (cyan) in wild-type (control) and $\beta1^{glo}$/NK-TGCK double-transgenic embryo hearts at E12.5. Scale bars, 100 μm. (**g**) Dot and box plot of the thickness of the left ventricle (LV) compact layer in control and $\beta1^{glo}$/NK-TGCK double-transgenic embryo (DTG2−) hearts without DOX treatment at E12.5. (**h**) DTG2− embryo hearts showed a significant decrease in the percentage of $Ki67^+$ cardiomyocytes in the compact layer at E12.5. (**i**) Dot and box plot of the thickness of the left ventricle (LV) compact layer in control and DOX-treated $\beta1^{glo}$/NK-TGCK double-transgenic embryo (DTG2+) hearts at E12.5. (**j**) DTG2+ embryo hearts showed a significant decrease in the percentage of $Ki67^+$ cardiomyocytes in the compact layer at E12.5. v, ventricle; I, first pharyngeal arch; II, second pharyngeal arch; Ib, limb bud. $^*P < 0.05$, $^{***}P < 0.005$; NS, not significant in unpaired two-tailed *t*-test. The bar graphs show the mean and error bars represent s.e.m. The box plot shows the median, with upper and lower percentiles, and the bars show maxima and minima values. Statistics source data can be found in Supplementary Table 12.

downstream targets of TBX20. PRDM16, a repressor of TGF-β signalling and a known genetic cause of LVNC and DCM, was significantly downregulated in all LVNC iPSC-CMs, TBX20KD-H7-CMs and the Tbx20 knockout mouse heart (Figs 5d and 6h,i). A previous genetic study of human LVNC with the PRDM16 mutation also revealed that truncation in exon 9 of PRDM16 is associated with the LVNC phenotype[12]. To confirm whether LVNC iPSC-CMs with the PRDM16 mutation showed abnormal activation of TGF-β signalling and a proliferation defect, as seen in LVNC iPSC-CMs with the TBX20 mutation, we next generated a genome-edited iPSC line carrying the frameshift mutation in exon 9 of the PRDM16 gene (PRDM16fs) and induced cardiac differentiation (Fig. 6j). Importantly, PRDM16fs iPSC-CMs showed significantly decreased proliferative response when exposed to growth factors and upregulation of TGF-β downstream

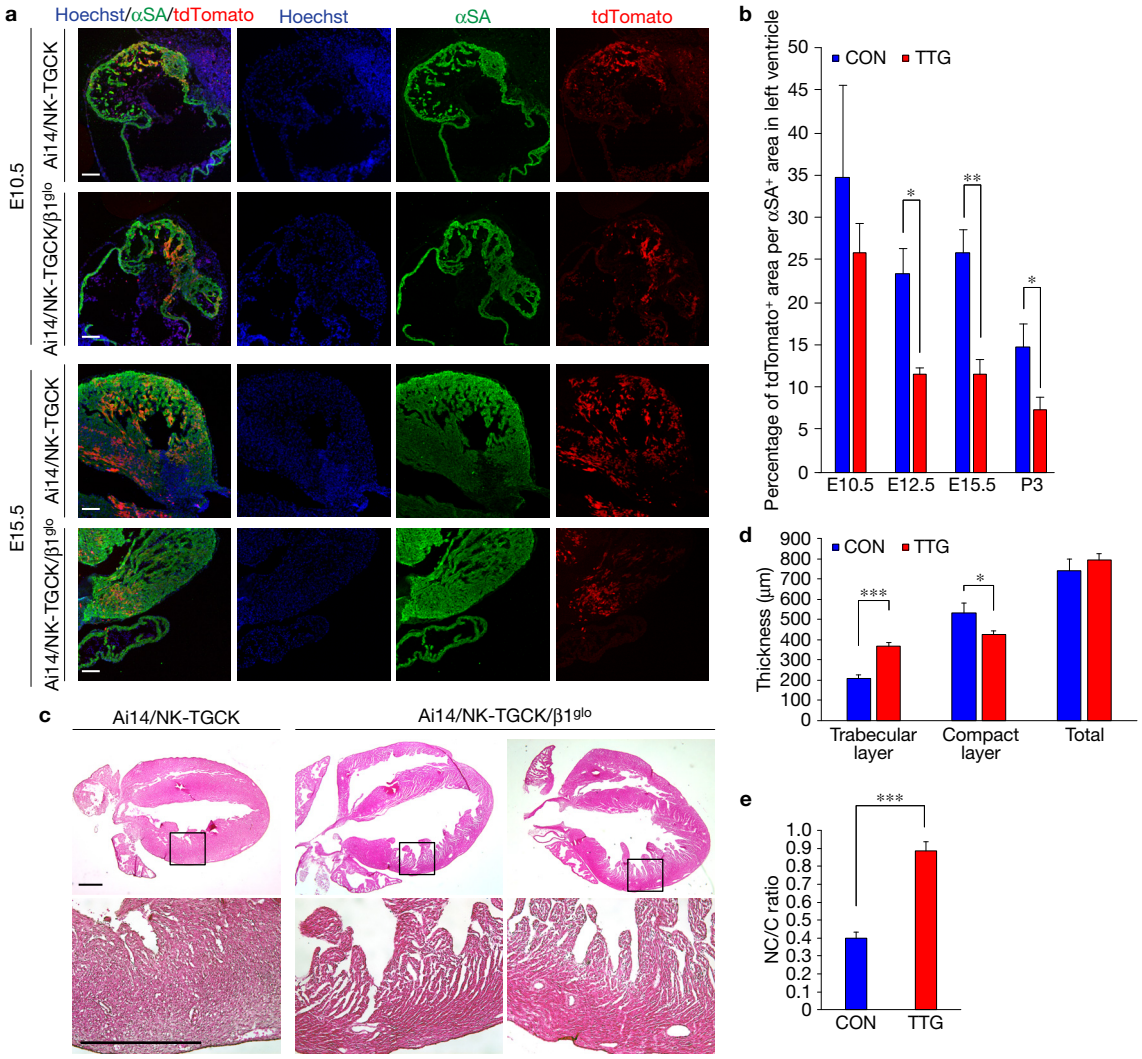

Figure 4 Disturbed expansion of embryonic cardiomyocytes and trabecular/compact layer ratio in the left ventricle of the TGF-β1-overexpressing mouse. (**a**) Immunostaining of nuclear (blue), tdTomato (red) and αSA (green) in coronal sections of control (Ai14/NK-TGCK) and Ai14/NK-TGCK/β1^{glo} triple-transgenic embryo hearts with doxycycline treatment at E10.5 and E15.5. Scale bars, 100 μm. (**b**) Percentage of tdTomato-positive area per αSA-positive area in the compact layer of control and Ai14/NK-TGCK/β1^{glo} triple-transgenic (TTG) mouse hearts with doxycycline treatment at E10.5 (control, $n=5$ hearts; triple-transgenic, $n=5$ hearts), E12.5 (control, $n=6$ hearts; triple-transgenic, $n=5$ hearts), E15.5 (control, $n=6$ hearts; triple-transgenic, $n=5$ hearts), and postnatal day 3 (P3) (control, $n=18$ hearts; triple-transgenic, $n=8$ hearts). (**c**) Haematoxylin and eosin staining in coronal sections of control (CON: Ai14/NK-TGCK) and Ai14/NK-TGCK/β1^{glo} triple-transgenic mouse hearts with doxycycline treatment at postnatal day (P) 3. The lower panels show magnified views of areas indicated by the black box in the upper panels. (**d**) Thickness of the trabecular and compact layer and total myocardium in control ($n=8$ hearts) and Ai14/NK-TGCK/β1^{glo} triple-transgenic mouse ($n=11$ hearts) hearts with doxycycline treatment at P3. (**e**) Trabecular layer/compact layer (NC/C) ratio in control ($n=8$ hearts) and Ai14/NK-TGCK/β1^{glo} triple-transgenic mouse hearts ($n=11$ hearts) with doxycycline treatment at P3. Scale bars, 0.5 mm. $^{*}P<0.05$, $^{**}P<0.01$, $^{***}P<0.005$ in unpaired two-tailed t-test. The bar graphs show the mean and error bars represent s.e.m. Statistics source data can be found in Supplementary Table 12.

target genes (Fig. 6k,l). Furthermore, the explanted heart tissue of proband no. 1 showed a significant decrease of PRDM16 expression compared with control donor heart tissue (Fig. 6m), suggesting that the TBX20–PRDM16–TGF-β axis as one of the mechanisms causing LVNC.

Modification of TGF-β signalling or genetic correction of the TBX20 mutation exacerbate the proliferation defect in LVNC iPSC-CMs

Finally, we evaluated whether modification of aberrant TGF-β signalling could rescue the proliferation defect in LVNC iPSC-CMs. Inhibition of TGF-β signalling with TGF-β receptor-1 inhibitors or overexpression of a dominant-negative form of TGF-β receptor-2 increased S-phase cells in both LVNC iPSC-CMs and TBX20KD-H7-CMs compared with untreated cells (Fig. 7a–c and Supplementary Fig. 6). Likewise, knockdown of the downstream effector CDKN1A also improved the distribution of S-phase LVNC iPSC-CMs (Fig. 7d–f). To validate the effects of the TBX20 Y317* mutation on the phenotype of LVNC iPSC-CMs, we generated TBX20 Y317* mutation-corrected (LVNC-corrected) iPSCs from the proband's iPSCs (Supplementary Fig. 7a–e). LVNC-corrected iPSC-CMs showed increased cardiac differentiation efficiency, expression of

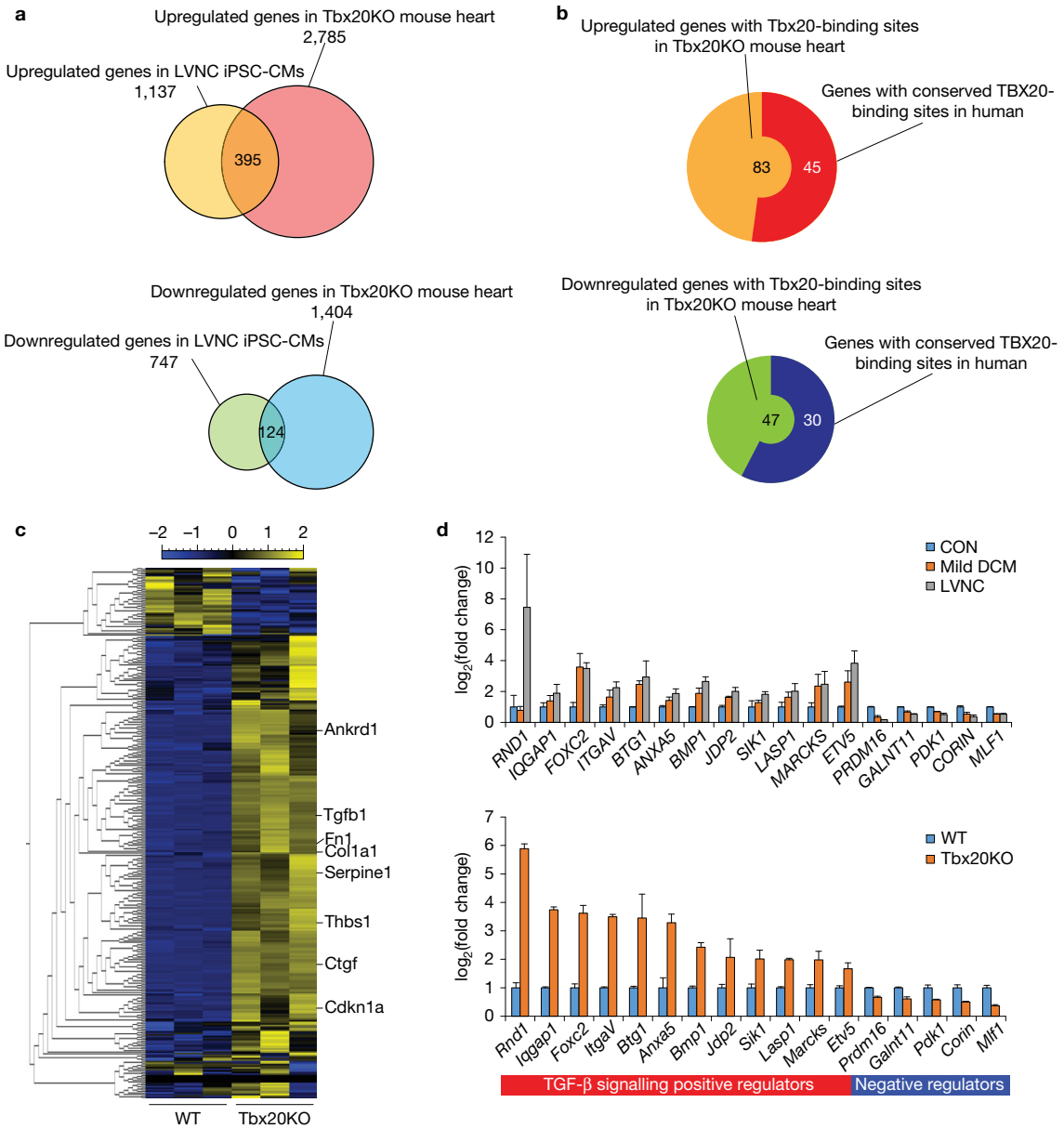

Figure 5 TBX20 regulates the expression of TGF-β signalling modifier genes in developing cardiomyocytes. (**a**) Venn diagram to show the overlap between genes upregulated (upper) or downregulated (lower) in LVNC iPSC-CMs compared with control iPSC-CMs ($q < 0.05$ following Benjamini–Hochberg correction), and genes upregulated (upper) or downregulated (lower) in Tbx20 knockout (Tbx20KO) mouse heart compared with the wild type ($q < 0.05$). The mouse data were obtained from the NCBI GEO database (http://www.ncbi.nlm.nih.gov/geo/query/acc.cgi?acc=GSE30943)[31]. (**b**) Predicted number of upregulated (upper) or downregulated (lower) genes with Tbx20-binding sites in Tbx20KO mouse heart and number of genes with a conserved Tbx20-binding site between mouse and human. The ChIP-sequencing data were obtained from the NCBI GEO database (http://www.ncbi.nlm.nih.gov/geo/query/acc.cgi?acc=GSM734426). (**c**) The heat map of the TGF-β signalling pathway showing upregulation of the TGF-β signalling pathway in Tbx20KO mouse heart compared with wild-type mouse heart. Mean = 0, variance = 1. (**d**) Significant mRNA expression changes of TBX20 downstream target genes that are involved in the TGF-β signalling pathway as validated by RNA-sequencing. These genes were found to have conserved binding sites in both human (LVNC versus control iPSC-CMS; upper) and mouse (Tbx20KO versus wild-type mouse heart; lower). The bar graphs show the mean and error bars represent s.e.m.

cardiac transcription factors, and restored proliferative capacity compared with non-corrected LVNC iPSC-CMs along with decreased TGF-β signalling activity (Fig. 7g–k). These results suggest that the TBX20 mutation contributes to the pathological phenotype of LVNC iPSC-CMs via disturbance of TGF-β signalling, which is associated with developmental defects of the compact layer during embryogenesis (Supplementary Fig. 7f).

DISCUSSION

Previously, both accelerative[9,11] and decelerative proliferation[5–7,12] in embryonic cardiomyocytes have been reported in animal models. In our transgenic mouse model, high overexpression of TGFB1 in the developing myocardium led to a severe developmental arrest in the compact layer and the severity of this non-compaction phenotype was directly correlated with the levels of TGFB1 overexpression. These

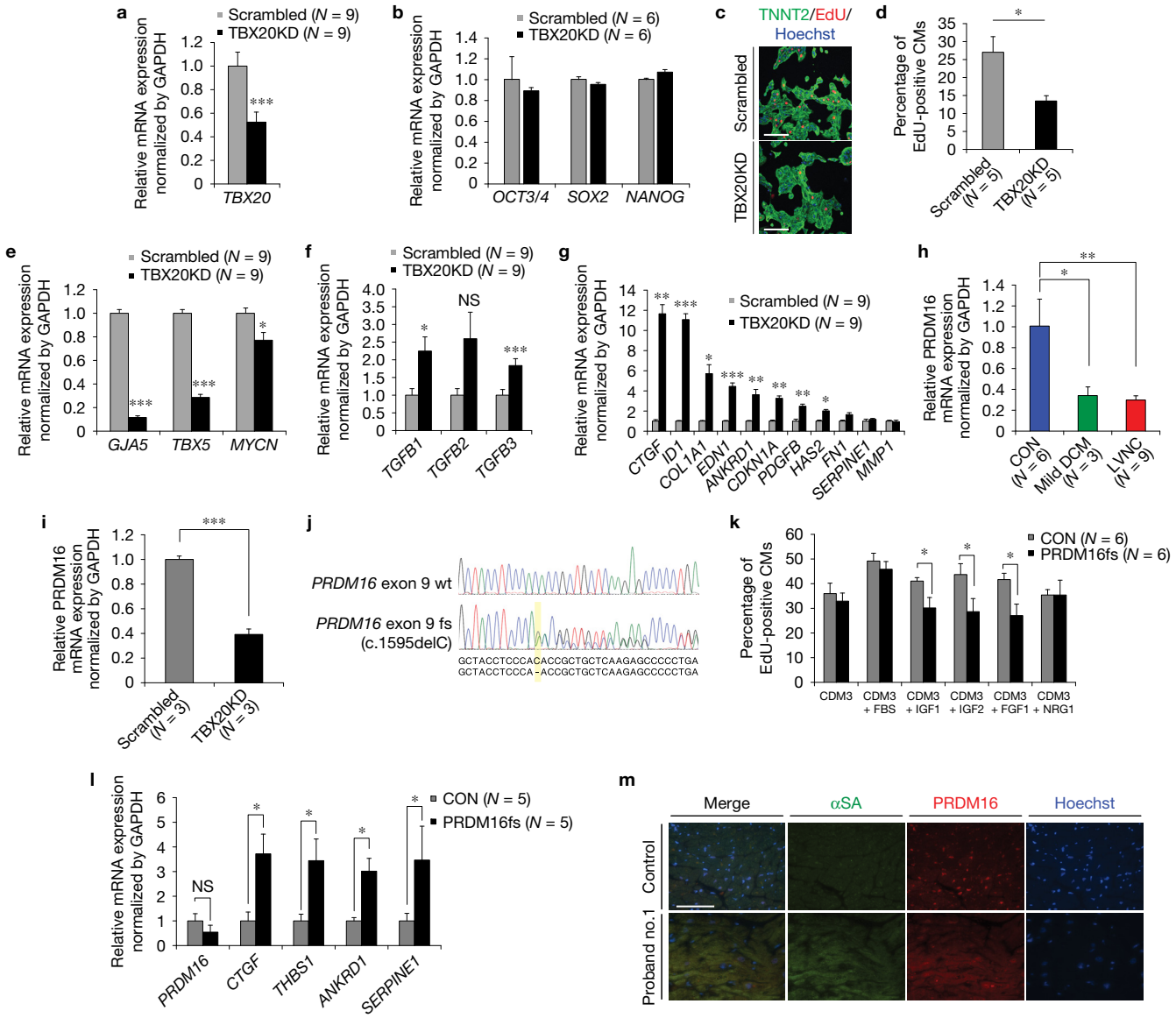

Figure 6 *PRDM16* is a candidate target gene of TBX20 in cardiomyocytes. (**a**) Validation of TBX20 shRNA knockdown efficiency in lentiviral TBX20 shRNA-transduced H7 ESC-CMs (TBX20KD) compared with scrambled shRNA-transduced H7 ESC-CMs (Scrambled) at 2 weeks. $n=9$ independent experiments per group. (**b**) Validation of pluripotent gene expression profile in TBX20KD and scrambled ESCs by qRT–PCR. (**c**) Immunostaining of nuclear (blue), TNNT2 (green), and EdU (red) in scrambled and TBX20KD ESC-CMs at 2 weeks. (**d**) Percentage of EdU$^+$ ESC-CMs in scrambled and TBX20KD ESC-CMs at 2 weeks. (**e**) Significant decrease of TBX20 downstream target gene (*GJA5*, *TBX5* and *MYCN*) expression in TBX20KD ESC-CMs compared with scrambled ESC-CMs at 2 weeks. (**f**,**g**) Significant increase of TGF-β isoforms (**f**) and TGF-β downstream target gene (**g**) expression in TBX20KD ESC-CMs compared with scrambled ESC-CMs at 2 weeks. (**h**,**i**) Significant decrease of PRDM16 mRNA expression in LVNC iPSC-CMs compared with control iPSC-CMs (**h**) and in TBX20KD-H7-CMs compared with scrambled H7-CMs (**i**). (**j**) CRISPR–Cas9-based frameshift mutation in exon 9 of the *PRDM16* gene in control iPSC lines (PRDM16 p.T532fs*8, c.1595delC: highlighted in yellow). wt, wild-type. (**k**) Percentage of EdU$^+$ cardiomyocytes in control and PRDM16 frameshift mutation-created iPSC-CMs (PRDM16fs) with or without growth factors. (**l**) Significant increase of TGF-β downstream target gene expression in PRDM16fs iPSC-CMs. (**m**) Immunostaining of nuclear (blue), alpha-sarcomeric actin (green) and PRDM16 (red) in LV of donor's control heart tissue and explanted heart of proband no. 1. CON, unrelated controls. $^*P<0.05$. $^{**}P<0.01$. $^{***}P<0.001$; NS, not significant in unpaired two-tailed *t*-test or one-way ANOVA followed by Tukey *post hoc* test. The bar graphs show the mean and error bars represent s.e.m. Scale bars, 100 μm. Statistics source data can be found in Supplementary Table 12.

observations suggest that at the early developmental stage of LV compact layer remodelling, proper activation of TGF-β signalling in the embryonic heart is required to ensure normal ventricular development.

Human iPSC-CMs have been used to model familial DCM[23,32,33], familial hypertrophic cardiomyopathy[34,35], long QT syndrome[36,37], and chemotherapy-induced cardiomyopathy[38], among others[39]. In this study, we demonstrate that iPSC-CM technology is useful not only for delineating the detailed molecular pathogenesis of congenital developmental defects, but also to clarify genetic causes in such diseases. We successfully found an association between functional disturbance of TBX20 and ectopic activation of TGF-β signalling in

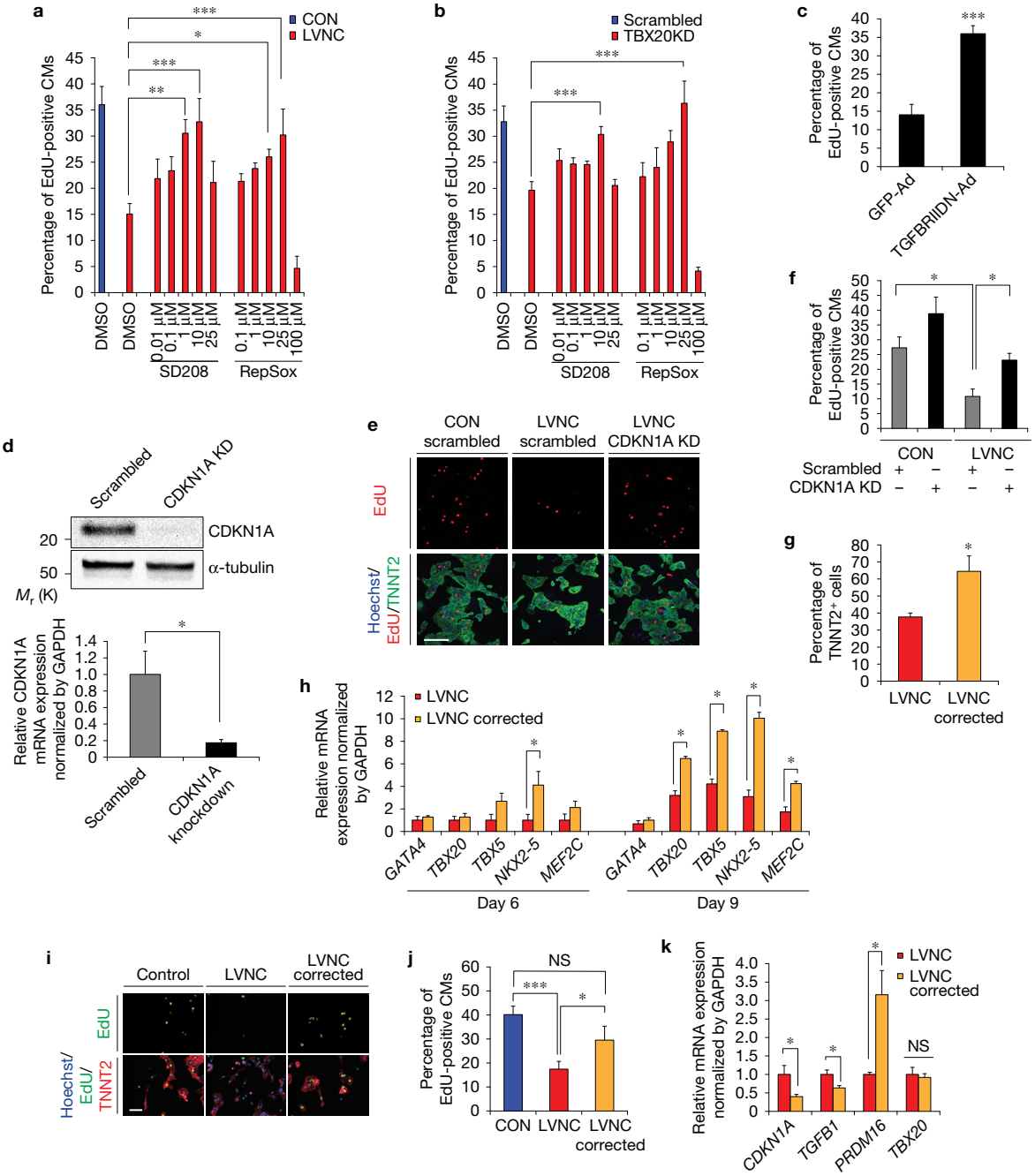

Figure 7 Rescue of pathological features of LVNC iPSC-CMs. (**a**,**b**) Percentage of EdU$^+$ control and LVNC iPSC-CMs (**a**) or scrambled control and TBX20 knockdown ESC-CMs (**b**) at 2 weeks after induction of cardiac differentiation with or without treatment of TGF-β receptor-1 inhibitors (SD208 or RepSox) for 2 continuous days. $n=7$ independent experiments. (**c**) Adenoviral-mediated overexpression of a dominant-negative form of TGF-β receptor-2 (TGFBRIIDN) significantly restored proliferative potential in LVNC iPSC-CMs compared with the control (adenoviral-mediated GFP overexpression, GFP-Ad). $n=8$ independent experiments. (**d**) Knockdown efficiency of CDKN1A protein (upper) and mRNA (lower) in iPSC-CMs by siRNA. $n=6$ independent experiments. (**e**) Immunostaining for nuclear (blue), TNNT2 (green) and EdU (red) in control and LVNC iPSC-CMs with CDKN1A or scramble siRNA knockdown. (**f**) Percentage of EdU$^+$ iPSC-CMs at 2 weeks after induction of cardiac differentiation with CDKN1A or scramble siRNA knockdown. $n=6$ independent experiments. (**g**) The efficiency of cardiac differentiation of LVNC and mutation-corrected LVNC iPSC lines before glucose deprivation as validated by FACS for TNNT2. $n=5$ independent experiments per group. (**h**) mRNA expression of cardiac transcription factors in differentiating LVNC and mutation-corrected LVNC iPSCs at day 6 and day 9 after induction of cardiac differentiation. LVNC: $n=6$ independent experiments; LVNC corrected: $n=5$ independent experiments. (**i**) Immunostaining for nuclear (blue), TNNT2 (red) and EdU (green) in control, LVNC and TBX20 mutation-corrected (LVNC corrected) iPSC-CMs. (**j**) Percentage of EdU$^+$ iPSC-CMs at 2 weeks in the control, LVNC and LVNC-corrected group. $n=6$ independent experiments. (**k**) Reversible CDKN1A, TGFB1 and PRDM16 mRNA expression abnormality in LVNC-corrected iPSC-CMs compared with LVNC iPSC-CMs. $n=6$ independent experiments. CON, unrelated controls. Scale bars, 100 μm. $^*P<0.05$, $^{**}P<0.01$, $^{***}P<0.005$; NS, not significant in unpaired two-tailed *t*-test or one-way ANOVA followed by Tukey *post hoc* test. The bar graphs show the mean and error bars represent s.e.m. Statistics source data can be found in Supplementary Table 12. Unprocessed original scans of blots are shown in Supplementary Fig. 8.

patient-specific iPSC-CMs as well as perturbed regulation of putative downstream targets of TBX20. We showed that *PRDM16* is a possible downstream target gene of TBX20. PRDM16 is a known cause of LVNC in humans and morpholino knockdown of PRDM16 causes a proliferation defect in the developing zebrafish heart[12]. PRDM16 is a repressor of TGF-β signalling[40–42] via binding of SMAD2/3, and our results revealed ectopic activation of TGF-β signalling in LVNC iPSC-CMs consistent with these previous studies. Although the comprehensive RNA expression data and ChIP-sequencing data showed that TBX20 has a large number of potential downstream target genes associated with TGF-β signalling regulation, our data suggest that the TBX20/PRDM16/TGF-β signalling pathway may be one of the key regulatory cascades for proper development of the compact/trabecular layer.

It is known that patients with LVNC generally show a wide spectrum of clinical manifestations. Some are asymptomatic, and the age at presentation can vary considerably, from as early as the newborn period to as late as older adulthood[43,44]. This may be explained by varying expression levels of mutant allele-specific mRNA expression between mild DCM and LVNC as shown here. TBX20 is known to interact with other cardiac transcription factors including NKX2-5, GATA4 and TBX5 that are essential for embryonic cardiomyocyte proliferation and ventricular development. As shown here, the disturbance of the interaction between TBX20 and these cardiac transcription factors may negatively impact the expansion of embryonic cardiomyocytes and impair the formation of the multilayered compact myocardium (Supplementary Fig. 7f). The differences of allele-specific TBX20 expression and the background expression of these cardiac transcription factors that may also be affected by heterogeneous factors could then impact the various cardiac phenotypes in patients with TBX20 mutations.

In conclusion, iPSC-CMs recapitulate the proliferative defects associated with LVNC[5–7,12] at the single-cell level. Importantly, this study presents the supporting evidence of a proliferation defect, a consequence of abnormal activation of TGF-β signalling, as a pathological feature of human LVNC. Whether this defect is common to all cases of LVNC or just a genetic subset remains to be determined. Our data suggest that iPSC-CMs may be useful in therapeutic screening to identify potential interventions for this cardiomyopathy in the future. □

METHODS

Methods, including statements of data availability and any associated accession codes and references, are available in the online version of this paper.

Note: Supplementary Information is available in the online version of the paper

ACKNOWLEDGEMENTS

We thank N. Sun, S. Hu and J. Lee for their help with functional assessments; H. Yamagishi (Keio University, Japan) for providing plasmid; A. B. Glick (Pennsylvania State University, USA) for providing dominant-negative TGFBRII overexpression adeno virus; B. Huber, B. Patlolla and G. Berry for their help with analysing the *in vivo* study. We are grateful for the support provided by the Neuroscience Microscopy Service (NMS), and FACS Core at the Institute for Stem Cell Biology and Regenerative Medicine, Stanford University. This work is supported by the Uehara Memorial Foundation Research Fellowship, American Heart Association Postdoctoral Fellowship 15POST25160016 (K.K.), American Heart Association Postdoctoral Fellowship 15POST22940013 and NIH K99HL130416 (S.-G.O.), The Ministry of Education, Culture, Sports, Science and Technology in Japan (F.I.), National Institutes of Health P01 GM099130 (M.P.S.), NIH K18 HL11708301, Children's Cardiomyopathy Foundation (D.B.), AHA Established Investigator Award, NIH R01 HL113006, NIH R01 HL130020, NIH R01 126527, NIH R01 128170, NIH R01 HL123968 and NIH R24 HL117756 (J.C.W.).

AUTHOR CONTRIBUTIONS

All authors have read and approved the manuscript. K.K., S.-G.O., D.B. and J.C.W. designed research, performed the experiments and wrote the manuscript; F.I., D.B. and J.C.W. recruited the patients; K.K., J.M.C. and S.-G.O. generated and performed experiments on iPSCs/ESCs with the help of A.D.E. and G.J.; K.K., F.J., K.H., K.I. and J.M.C. performed sequencing and bioinformatics analysis; S.M.W. generated NK-TGCK transgenic mouse; K.K., V.T. and I.K. generated genome-corrected iPSC lines; K.K., P.S. and O.J.A. performed and interpreted the patch clamping and calcium imaging data; M.P.S. provided scientific advice; and J.C.W. provided funding and supervised the entire research project.

COMPETING FINANCIAL INTERESTS

J.C.W. is co-founder of Stem Cell Theranostics. The remaining authors declare no competing financial interests.

Published online at http://dx.doi.org/10.1038/ncb3411
Reprints and permissions information is available online at www.nature.com/reprints

1. Kohli, S. K. *et al.* Diagnosis of left-ventricular non-compaction in patients with left-ventricular systolic dysfunction: time for a reappraisal of diagnostic criteria? *Eur. Heart J.* **29,** 89–95 (2008).
2. Nugent, A. W. *et al.* The epidemiology of childhood cardiomyopathy in Australia. *N. Engl. J. Med.* **348,** 1639–1646 (2003).
3. Sedmera, D., Pexieder, T., Vuillemin, M., Thompson, R. P. & Anderson, R. H. Developmental patterning of the myocardium. *Anat. Rec.* **258,** 319–337 (2000).
4. Chin, T. K., Perloff, J. K., Williams, R. G., Jue, K. & Mohrmann, R. Isolated noncompaction of left ventricular myocardium. A study of eight cases. *Circulation* **82,** 507–513 (1990).
5. Kosaka, Y. *et al.* 14-3-3epsilon plays a role in cardiac ventricular compaction by regulating the cardiomyocyte cell cycle. *Mol. Cell. Biol.* **32,** 5089–5102 (2012).
6. Chen, Q. *et al.* Smad7 is required for the development and function of the heart. *J. Biol. Chem.* **284,** 292–300 (2009).
7. DiMichele, L. A. *et al.* Transient expression of FRNK reveals stage-specific requirement for focal adhesion kinase activity in cardiac growth. *Circ. Res.* **104,** 1201–1208 (2009).
8. Bartram, U. *et al.* Double-outlet right ventricle and overriding tricuspid valve reflect disturbances of looping, myocardialization, endocardial cushion differentiation, and apoptosis in TGF-β2-knockout mice. *Circulation* **103,** 2745–2752 (2001).
9. Shou, W. *et al.* Cardiac defects and altered ryanodine receptor function in mice lacking FKBP12. *Nature* **391,** 489–492 (1998).
10. Grego-Bessa, J. *et al.* Notch signaling is essential for ventricular chamber development. *Dev. Cell* **12,** 415–429 (2007).
11. Luxan, G. *et al.* Mutations in the NOTCH pathway regulator MIB1 cause left ventricular noncompaction cardiomyopathy. *Nat. Med.* **19,** 193–201 (2013).
12. Arndt, A. K. *et al.* Fine mapping of the 1p36 deletion syndrome identifies mutation of PRDM16 as a cause of cardiomyopathy. *Am. J. Hum. Genet.* **93,** 67–77 (2013).
13. Chakraborty, S. & Yutzey, K. E. Tbx20 regulation of cardiac cell proliferation and lineage specialization during embryonic and fetal development *in vivo*. *Dev. Biol.* **363,** 234–246 (2012).
14. Takeuchi, J. K. *et al.* Tbx20 dose-dependently regulates transcription factor networks required for mouse heart and motoneuron development. *Development* **132,** 2463–2474 (2005).
15. Hammer, S. *et al.* Characterization of TBX20 in human hearts and its regulation by TFAP2. *J. Cell. Biochem.* **104,** 1022–1033 (2008).
16. Posch, M. G. *et al.* A gain-of-function TBX20 mutation causes congenital atrial septal defects, patent foramen ovale and cardiac valve defects. *J. Med. Genet.* **47,** 230–235 (2010).
17. Liu, C. *et al.* T-box transcription factor TBX20 mutations in Chinese patients with congenital heart disease. *Eur. J. Med. Genet.* **51,** 580–587 (2008).
18. Qian, L. *et al.* Transcription factor neuromancer/TBX20 is required for cardiac function in *Drosophila* with implications for human heart disease. *Proc. Natl Acad. Sci. USA* **105,** 19833–19838 (2008).
19. Kirk, E. P. *et al.* Mutations in cardiac T-box factor gene TBX20 are associated with diverse cardiac pathologies, including defects of septation and valvulogenesis and cardiomyopathy. *Am. J. Hum. Genet.* **81,** 280–291 (2007).
20. Chen, G. *et al.* Chemically defined conditions for human iPSC derivation and culture. *Nat. Methods* **8,** 424–429 (2011).
21. Churko, J. M., Burridge, P. W. & Wu, J. C. Generation of human iPSCs from human peripheral blood mononuclear cells using non-integrative Sendai virus in chemically defined conditions. *Methods Mol. Biol.* **1036,** 81–88 (2013).
22. Burridge, P. W. *et al.* Chemically defined generation of human cardiomyocytes. *Nat. Methods* **11,** 855–860 (2014).

23. Wu, H. *et al.* Epigenetic regulation of phosphodiesterases 2A and 3A underlies compromised β-adrenergic signaling in an iPSC model of dilated cardiomyopathy. *Cell Stem Cell* **17,** 89–100 (2015).
24. D'Amato, G. *et al.* Sequential Notch activation regulates ventricular chamber development. *Nat. Cell Biol.* **18,** 7–20 (2016).
25. Engelmann, G. L., Boehm, K. D., Birchenall-Roberts, M. C. & Ruscetti, F. W. Transforming growth factor-β 1 in heart development. *Mech. Dev.* **38,** 85–97 (1992).
26. Kitamura, R. *et al.* Stage-specific role of endogenous Smad2 activation in cardiomyogenesis of embryonic stem cells. *Circ. Res.* **101,** 78–87 (2007).
27. Hauck, L. *et al.* Critical role for FoxO3a-dependent regulation of p21CIP1/WAF1 in response to statin signaling in cardiac myocytes. *Circ. Res.* **100,** 50–60 (2007).
28. Akli, S., Zhan, S., Abdellatif, M. & Schneider, M. D. E1A can provoke G1 exit that is refractory to p21 and independent of activating Cdk2. *Circ. Res.* **85,** 319–328 (1999).
29. Brooks, G., Poolman, R. A. & Li, J. M. Arresting developments in the cardiac myocyte cell cycle: role of cyclin-dependent kinase inhibitors. *Cardiovasc. Res.* **39,** 301–311 (1998).
30. Madisen, L. *et al.* A robust and high-throughput Cre reporting and characterization system for the whole mouse brain. *Nat. Neurosci.* **13,** 133–140 (2010).
31. Sakabe, N. J. *et al.* Dual transcriptional activator and repressor roles of TBX20 regulate adult cardiac structure and function. *Hum. Mol. Genet.* **21,** 2194–2204 (2012).
32. Sun, N. *et al.* Patient-specific induced pluripotent stem cells as a model for familial dilated cardiomyopathy. *Sci. Transl. Med.* **4,** 130ra147 (2012).
33. Davis, J. *et al.* A tension-based model distinguishes hypertrophic versus dilated cardiomyopathy. *Cell* **165,** 1147–1159 (2016).
34. Lan, F. *et al.* Abnormal calcium handling properties underlie familial hypertrophic cardiomyopathy pathology in patient-specific induced pluripotent stem cells. *Cell Stem Cell* **12,** 101–113 (2013).
35. Hinson, J. T. *et al.* Titin mutations in iPS cells define sarcomere insufficiency as a cause of dilated cardiomyopathy. *Science* **349,** 982–986 (2015).
36. Itzhaki, I. *et al.* Modelling the long QT syndrome with induced pluripotent stem cells. *Nature* **471,** 225–229 (2011).
37. Wang, Y. *et al.* Genome editing of isogenic human induced pluripotent stem cells recapitulates long QT phenotype for drug testing. *J. Am. Coll. Cardiol.* **64,** 451–459 (2014).
38. Burridge, P. W. *et al.* Human induced pluripotent stem cell-derived cardiomyocytes recapitulate the predilection of breast cancer patients to doxorubicin-induced cardiotoxicity. *Nat. Med.* **22,** 547–556 (2016).
39. Matsa, E., Ahrens, J. H. & Wu, J. C. Human induced pluripotent stem cells as a platform for personalized and precision cardiovascular medicine. *Physiol. Rev.* **96,** 1093–1126 (2016).
40. Takahata, M. *et al.* SKI and MEL1 cooperate to inhibit transforming growth factor-β signal in gastric cancer cells. *J. Biol. Chem.* **284,** 3334–3344 (2009).
41. Warner, D. R. *et al.* PRDM16/MEL1: a novel Smad binding protein expressed in murine embryonic orofacial tissue. *Biochim. Biophys. Acta* **1773,** 814–820 (2007).
42. Bjork, B. C., Turbe-Doan, A., Prysak, M., Herron, B. J. & Beier, D. R. Prdm16 is required for normal palatogenesis in mice. *Hum. Mol. Genet.* **19,** 774–789 (2010).
43. Oechslin, E. & Jenni, R. Left ventricular non-compaction revisited: a distinct phenotype with genetic heterogeneity? *Eur. Heart J.* **32,** 1446–1456 (2011).
44. Sen-Chowdhry, S. & McKenna, W. J. Left ventricular noncompaction and cardiomyopathy: cause, contributor, or epiphenomenon? *Curr. Opin. Cardiol.* **23,** 171–175 (2008).

METHODS

Derivation of human induced pluripotent stem cells (iPSCs). Fibroblasts or peripheral blood mononuclear cells (PBMCs) were obtained from family members with LVNC with informed consent under protocols approved by the Stanford University Human Subjects Research Institutional Review Board. Human skin-punch biopsies were digested with collagenase II and transferred into 6-well culture dish (BD Biosciences). At passage 2 or later, primary fibroblasts were used for reprogramming to iPSCs using the non-integrating Sendai virus-based CytoTune-iPS Reprogramming Kit (Life Technologies). After 24 h and 72 h, the medium was replaced. At day 4, cells were detached using TrypLE (Life Technologies) and replated onto mouse embryonic fibroblast (MEF)-coated 6-well plates in DMEM/GlutaMAX with 10% FBS and Rho-associated, coiled-coil containing protein kinase (ROCK) inhibitor, Y27632 (Selleckchem). From day 5 onwards, cells were cultured in mTeSR medium (STEMCELL Technologies). Colonies were picked after day 20 and transferred to a Matrigel-coated culture dish (BD Biosciences), and subsequently passaged using Accutase (Global Cell Solutions). After passage 10, the culture medium was changed to Essential 8 (Life Technologies)[20]. PBMC reprogramming was performed as described previously[21]. Briefly, PBMCs were isolated using a Ficoll-Paque Premium (GE Healthcare) from 20 ml of whole blood and plated at 1 million cells per millilitre in 2 ml of blood medium[21]. After day 9, 1×10^6 cells were plated in blood medium with Sendai virus. Cells were transferred to mTeSR medium in a MEF-coated 6-well plate at day 3. Colonies were picked after day 20 and transferred to a new Matrigel-coated culture dish and cultured as described above.

Culture and maintenance of iPSCs and ESCs. Human ESCs and iPSCs were grown on Matrigel-coated plates using chemically defined E8 medium as described before[20]. The medium was changed daily and cells were passaged every 4 days using EDTA.

Cardiac differentiation. iPSCs were grown to 90% confluence and differentiated subsequently into beating cardiomyocytes, using a small-molecule-based monolayer method described in detail previously[22]. Ten days after cardiac differentiation, iPSC-CM monolayers were purified using RPMI-1640 without glucose (Life Technologies) with B27 supplement (Life Technologies). Non-glucose culture medium was changed every 2 days. After 5 days, iPSC-CMs were reseeded onto Matrigel-coated plates in culture medium with glucose.

Pluripotency marker analysis. Human ESC and iPSC colonies grown in Matrigel-coated 8-well chamber glasses (Thermo Scientific) were fixed using 4% paraformaldehyde (PFA) and permeabilized with 0.5% Triton X-100. After blocking samples with 5% goat serum in PBST (PBS with 0.1% Tween20), cells were stained with mouse anti-SSEA4 (R&D systems), rabbit anti-OCT3/4 (Santa Cruz Biotechnology), rabbit anti-NANOG (Santa Cruz Biotechnology) and mouse anti-TRA1-60 (EMD Millipore) antibodies. Cells were then incubated with Alexa Fluor-conjugated secondary antibodies (Life Technologies) and Hoechst 33342 (Life Technologies) to visualize the specific stains. Image acquisition was performed on an Eclipse 80i fluorescence microscope (Nikon Instruments).

Teratoma formation assay. iPSCs (1×10^6) were suspended in 25 µl PBS, mixed with equal volumes of Matrigel, and injected into the subcutaneous regions of the anterior thigh of immunodeficient female SCID mice ($n = 2$ spots per group of mice) (Charles River Laboratories). Fifty days after transplantation, teratomas were explanted, fixed with 4% paraformaldehyde, set in paraffin, sectioned, and stained with haematoxylin & eosin (H&E).

Plasmid construction and site-directed mutagenesis. The Flag-tagged human TBX20 expression vector (TBX20-pCMV tag2B), GATA4 expression vector (GATA4-pcDNA3.1), NKX2.5 expression vector (NKX2.5-pcDNA3.1), TBX5 expression vector (TBX5-pcDNA3.1), and the NPPA promoter luciferase reporter vector (NPPA-pGL3 basic) were provided by H. Yamagishi. Site-directed mutagenesis was performed using a QuikChange Site-Directed Mutagenesis Kit (Agilent Technologies) according to the manufacturer's instructions. The MSX2 promoter sequence containing a 3.9-kb fragment of the MSX2 5′ untranslated and flanking region was subcloned into pGL3-Basic (Promega), as described previously[45]. All constructed vectors were verified by sequencing.

Luciferase assay. The HeLa cells were purchased from ATCC. The cells were not authenticated or tested for mycoplasma contamination recently. No cell lines used in this study were found in the database of commonly misidentified cell lines that is maintained by ICLAC and NCBI Biosample. HeLa cells were transfected using Lipofectamine 2000 (Life Technologies) with 50 ng reporter vector, 50 ng expression vectors, and 0.2 ng pRL-SV40 internal control vector (Promega). Luciferase activity was measured 48 h after transient transfection by using Dual-Glo Luciferase Reporter Assay System (Promega) according to the manufacturer's instructions. Six independent assays were performed in duplicate.

Immunocytochemistry. Cells grown on coverslips were fixed using 4% PFA, permeabilized with 0.5% Triton X-100, incubated with primary antibodies and Hoechst 33342, and detected using Alexa Fluor-conjugated secondary antibodies. Primary antibodies used include mouse anti-FLAG M2 (Sigma-Aldrich), rabbit anti-cardiac troponin T (Abcam), mouse anti-cardiac troponin T (Thermo Scientific), or mouse anti-sarcomeric alpha-actinin (Sigma-Aldrich), as published previously[45]. Image acquisition was performed on an Eclipse 80i fluorescence microscope and a confocal microscope (Carl Zeiss, LSM 510 Meta) and ZEN software (Carl Zeiss). Measurement of cell surface area and length was performed using NIS-Elements Basic Research 3.0 software (Nikon). A detailed list of antibodies used is shown in Supplementary Table 10.

EdU-based proliferation analysis. iPSC-CMs were cultured in RPMI with B27 supplement and 2% FBS 2 days before EdU staining to accelerate the proliferation. Staining was performed using the Click-it EdU Imaging Kit (Life technologies) according to the manufacturer's instructions. EdU was incorporated for 24 h before the experiment. Cells were fixed with 4% PFA, permeabilized with 0.5% Triton X-100 in PBS, and stained with Alexa Fluor-conjugated azide. After washing and blocking with 5% goat serum in PBST, cells were incubated with a rabbit anti-TNNT2 antibody (Abcam) and visualized with anti-rabbit Alexa Fluor-conjugated secondary antibody and Hoechst 33342. At least more than one hundred cells were counted per sample and more than three independent studies per group were performed. Measurement of the fluorescent signals was performed using NIS-elements BR analysis 4.13.04 64-bit software (Nikon).

RNA-sequencing. Eight paired-end cDNA libraries (two biological replicates of proband iPSC-CMs, two biological replicates of father iPSC-CMs, one biological replicate of two sibling iPSC-CMs, and one biological replicate of two control iPSC-CMs) were prepared and sequenced. Total RNA was extracted and quantified using the miRNeasy Kit (Qiagen) according to the manufacturer's protocol. Ten micrograms of total RNA was used to generate index-tagged paired-end cDNA libraries. Briefly, mRNAs were purified by the polyA enrichment procedure using Dynal Oligo(dT) beads (Life technologies). mRNA fragmentation was performed using RNA Fragmentation Reagents (Life Technologies) to obtain 200–300 bp fragments. cDNA was generated using the SuperScript Double-Stranded cDNA Synthesis Kit (Life technologies). Illumina sequencing adapters were ligated to cDNA using LigaFast (Promega) and PE Adapter Oligo Mix (Illumina). PCR was performed on the adapter-ligated cDNA with 2X Phusion DNA polymerase Master Mix (New England Biolabs). Sequencing was performed with Illumina's HiSeq2000 or 2500 platform using paired-end reads at an average length of 100 bp (2×100).

RNA-seq data processing and differential expression analysis. Paired-end fastq sequence reads from each sample were assembled against hg19 using the Tophat v2.0.6 (http://tophat.cbcb.umd.edu) with the Illumina-supplied hg19 gene-model annotation file (gtf annotation). The expression level (FPKM, fragments per kilobase of exon per million fragments mapped) was estimated by Cufflinks (http://cufflinks.cbcb.umd.edu). The Q value is the same as the false discovery rate. Cuffdiff was used to call differentially expressed genes with a false discovery rate less than 0.05. Cuffdiff was run against the UCSC iGenomes GTF file from Illumina (http://cole-trapnell-lab.github.io/cufflinks//igenome_table/index.html). Subsequent to determining which genes were differentially expressed, FPKM was used for filtering and visualization purposes. Only genes with expression values >1 FPKM in at least one sample were considered for subsequent analysis. Samtools (http://samtools.sourceforge.net) was used to calculate allele-specific expression of the TBX20 gene. We used this software to analyse the differentially expressed genes between controls and LVNC patients. Using IPA Upstream Regulator analysis, the cascade of upstream transcriptional regulators was predicted, and this explained the observed gene expression changes. This upstream regulator analysis is based on prior knowledge of expected effects between transcriptional regulators and their target genes stored in the Ingenuity Knowledge Base. The activation z-score was validated to infer the activation states of predicted transcriptional regulators by the IPA Upstream Regulator analysis. The P value measures whether there is a statistically significant overlap between the data set genes and the genes that are regulated by a transcription regulator. The P value calculated using Fisher's exact test, and significance is generally attributed to $P < 0.01$. RNA and ChIP-sequencing data of wild-type and Tbx20 knockout mouse heart were obtained from the NCBI GEO database (RNA-sequencing: http://www.ncbi.nlm.nih.gov/geo/query/acc.cgi?acc=GSE30943, ChIP-sequencing: http://www.ncbi.nlm.nih.gov/geo/query/acc.cgi?acc=GSM734426)[31]. All of the RNA sequencing data can be accessed as the GEO reference GSE63161.

Quantifying allele-specific expression using RNA-seq data. Allele-specific expression of the TGFB gene was measured using RNA-Seq data. Alignment was performed using tophat v2.0.6 (http://tophat.cbcb.umd.edu) and processed using

DOI: 10.1038/ncb3411

SAMtools v0.1.2, which produces site-specific allele frequencies using overlapping reads (read pileup). Allele-specific expression was calculated by determining whether or not each overlapping read at mutant site fitted the reference or the mutant allele. These summed counts represented our measures of relative allelic abundance at that site. Any deviation from equal allelic abundance was reflected as allelic imbalance[46].

Quantitative RT-PCR. Total RNA was prepared using the RNAeasy plus kit (Qiagen). cDNA was synthesized by the High Capacity cDNA Reverse Transcription Kit (Life Technologies). Quantitative real-time polymerase chain reaction (qRT-PCR) was performed on a StepOne Real-Time PCR System (Life Technologies) using the TaqMan Universal PCR Master Mix (Life technologies) according to the manufacturer's protocol. Relative quantification was normalized against GAPDH. More than three respective sets of experiments were performed.

Digital droplet PCR for the detection and quantification of TBX20 wild-type and mutant allele-specific mRNA. Total RNA of 2-week-old LVNC and mild DCM iPSC-CMs was extracted and prepared using the RNAeasy plus kit (Qiagen). cDNA was synthesized by the High Capacity cDNA Reverse Transcription Kit (Life Technologies). The quantification of allele-specific mRNA expression was analysed using the QX100 Droplet Digital PCR system (Bio-Rad). The Y317* mutation was detected with an FAM probe: 5′-FAM-ZCCATCCGTACCTACGGAGGAGAX- Black Hole Quenche-3′, and the wild-type allele with another HEX probe: 5′-HEX-ZCCATCCG TACCTAAGGAGGAGAX- Black Hole Quencher-3′. Each reaction mix consisted of the following: 2× ddPCR Supermix, 20× specific target primers including the forward primer (5′-GGAAAGTGTGGAGAGCCTGA-3′) and the reverse primer (5′-TGACTCTCATCCCCCAAGAC-3′), 20× mutant-specific FAM probes, 20× wild-type-specific HEX-probe, 5 ng cDNA template, and the mixture was adjusted with PCR-grade water to a final volume of 20 µl. The thermal cycling conditions were as follows: enzyme activation, 95 °C for 10 min (1 cycle); denaturation, 94 °C for 30 s (40 cycles); annealing/extension, 61 °C for 1 min (40 cycles); and hold 98 °C for 10 min (1 cycle). The ddPCR data were analysed with QuantaSoft analysis software (Bio-Rad), and the quantification of either the deletion or the insertion allele was presented as the number of copies per microlitre of PCR mixture.

Western blotting. Following SDS–PAGE, proteins were transferred to 0.45 µm nitrocellulose membranes (Bio-Rad) using a mini Bio-Rad Mini PROTEAN 3 Cell system in NuPAGE transfer buffer (Life technologies). The membrane was then blocked in Membrane Blocking Solution (Life technologies) and incubated with primary antibody overnight at 4 °C. Blots were incubated with the appropriate secondary antibodies for 1 h at room temperature and visualized using the ECL Western Blotting Analysis System (GE Healthcare). Primary antibodies used were biotinylated SMAD2/3 (Cell Signaling), phospho-SMAD2/3 (Cell Signaling), CDKN1A (Cell Signaling), TBX20 (Sigma-Aldrich), and HRP-conjugated α−tubulin (Cell Signaling). A detailed list of the antibodies used is shown in Supplementary Table 10.

Ca^{2+} imaging. Briefly, 30-day-old iPSC-CMs were dissociated with TrypLE and reseeded on Matrigel-coated 22-mm round coverslips. The Fluo-4 Direct Calcium Assay kit was used (Life Technologies) as per the manufacturer's instructions. Fluo-4 loading solution was incubated with the cells at 37 °C for 30 min and fluorescence was measured at 495 ± 20 nm excitation and 515 ± 20 nm emission. Videos were taken of iPSC-CMs spontaneously beating or electrically field-stimulated at 1 and 2 Hz, 10 V cm^{-1}, and 10 ms biphasic pulse width. Measurements were taken on an AxioObserver Z1 inverted microscope (Carl Zeiss) equipped with a Lambda DG-4 300 W xenon light source (Sutter Instruments), an ORCA-ER CCD (charge-coupled device) camera (Hamamatsu), and AxioVison 4.7 software (Zeiss). All experiments were conducted at 37 °C with normal culture medium (RPMI-1640 with B27 supplement). The mean Ca^{2+} signals of ten paced beats were analysed with ImageJ software. More than three sets of experiments were performed.

Patch clamp. Whole-cell action potentials (APs) were recorded with the use of a standard patch-clamp technique, as previously described[22]. Briefly, cultured iPSC-CMs were plated on No. 18 mm glass coverslips (Warner Instruments) coated with Matrigel, placed in a RC-26C recording chamber (Warner Instruments), and mounted onto the stage of an inverted microscope (Nikon). The chamber was continuously perfused with warm (35–37 °C) extracellular solution (pH 7.4) of the following composition: (mM) 150 NaC1, 5.4 KCl, 1.8 $CaCl_2$, 1.0 $MgCl_2$, 1.0 Na pyruvate, 15 HEPES, and 15 glucose. Glass micropipettes were fabricated from standard wall borosilicate glass capillary tubes (Sutter BF 100-50-10, Sutter Instruments) using a programmable puller (P-97; Sutter Instruments) and filled with the following intracellular solution (pH 7.2): 120 KCl, 1.0 $MgCl_2$, 10 HEPES, 10 EGTA, and 3 Mg-ATP. A single beating cardiomyocyte was selected and APs were recorded in whole-cell current clamp mode using an EPC-10 patch-clamp amplifier (HEKA). Data were acquired using PatchMaster software (HEKA) and digitized at 1.0 kHz. The following criteria are used for classifying observed APs into ventricular-, atrial- and nodal-like iPSC-CMs. For ventricular-like, the criteria were a negative maximum diastolic membrane potential (<−50 mV), a rapid AP upstroke, a long plateau phase, AP amplitude >90 mV, and AP duration at 90% repolarization/AP duration at 50% repolarization (APD90/APD50) <1.4. For atrial-like, the criteria were an absence of a prominent plateau phase, a negative diastolic membrane potential (<−50 mV), and APD90/APD50 >1.7. For nodal-like, the criteria were a more positive MDP, a slower AP upstroke, a prominent phase 4 depolarization, and APD90/APD50 between 1.4 and 1.7[22].

Transgenic mice. αMHC-Cre mice[47], mTmG mice[48], and NK-TGCK mice[49] were previously described. The tdTomato reporter mice (Ai14)[30] and transgenic mice that conditionally express active TGF-β1 following genomic recombination by Cre recombinase ($\beta1^{glo}$)[50] were purchased from the Jackson Laboratory. All transgenic mice were backcrossed with C57BL6 background more than five times. αMHC-Cre mice and NK-TGCK mice were crossed with mTmG reporter transgenic mice to observe the Cre activity in embryonic heart. αMHC-Cre mice and NK-TGCK mice were also crossed with $\beta1^{glo}$ mice to obtain cardiac-specific TGF-β1-overexpression (αMHC-Cre/$\beta1^{glo}$ or NK-TGCK/$\beta1^{glo}$) double-transgenic embryos. Doxycycline (2 mg ml^{-1} plus 50 mg ml^{-1} sucrose) was administrated orally in the drinking water and replaced every 4 days. Pregnant female mice were treated with doxycycline from embryonic day 0.5 to 7.0. For the generation of the NK-TGCK/$\beta1^{glo}$ double-transgenic adult female mice, pregnant female mice were treated with doxycycline from embryonic day 0.5 to 12.5 to inactivate the NK-TGCK transgene during pregnancy. NK-TGCK/$\beta1^{glo}$ double-transgenic female mice were crossed with Ai14 male mice to obtain triple-transgenic embryos and neonates. All experimental procedures were approved by the ethics committee of Stanford University and were in accordance with the Guide for the Care and Use of Laboratory Animals (US National Institutes of Health).

Immunohistochemistry. Mouse embryos and neonates were collected, fixed in 4% PFA, embedded in OCT, and frozen in dry ice/hexane. Frozen sections were blocked with 5% goat serum, stained with mouse anti-TNNT2 (Thermo Scientific), mouse anti-sarcomeric alpha-actinin (Sigma-Aldrich), rabbit anti-TNNI3 (Santa Cruz), rabbit anti-TGF-β1 (Abcam), rabbit anti-Ki67 (Thermo Scientific), rabbit anti-phospho-Histone H3 (Cell Signaling Technology), and Hoechst 33342, and visualized using Alexa Fluor-conjugated secondary antibodies (Life Technologies). Image acquisition was performed on a Zeiss LSM510 Meta inverted confocal microscope (Carl Zeiss) or an Eclipse 80i fluorescent microscope (Nikon). Transgenes were detected by PCR from yolk sac DNA of embryos or tail DNA of neonatal pups. For human heart tissues, formalin-fixed paraffin-embedded tissue sections were rehydrated and autoclaved with citrate buffer, pH 6.0 (Sigma-Aldrich) and stained with rabbit anti-phospho-Smad2 (EMD Millipore), rabbit anti-PRDM16 (Abcam), mouse anti-sarcomeric alpha-actinin (Sigma-Aldrich) and Hoechst 33342, and visualized using Alexa Fluor-conjugated secondary antibodies (Life Technologies). Image acquisition was performed on an Eclipse 80i fluorescence microscope (Nikon). A detailed list of the antibodies used is shown in Supplementary Table 10.

Exome sequencing in case–parent trio. Exome sequencing was performed on patient and both parents using the Agilent SureSelectXT Human All Exon V4 (50 Mb) (Agilent Technologies). Briefly, 3 µg of genomic DNA was sheared in 130 µl of low-TE buffer to a peak size of 150–200 bp using Covaris E220, and then purified with AmpPure XP beads to remove fragments less than 100 bp. The purified DNA fragments were then subjected to the Agilent SureSelect Library preparation kit, ILM, to be end-repaired, A-tailed, and ligated to indexing-specific paired-end adapter. The adapter-ligated libraries were amplified for five cycles using Herculase II (Agilent Technologies). Amplified pre-capture libraries (750 ng) were concentrated in 3 µl and hybridized to the target specific baits (SureSelectXT Human All Exon V4; Agilent Technologies) according to the manufacturer's recommendations. Hybridized material was captured using streptavidin-coated beads (Invitrogen) and amplified for 10 cycles. Captured libraries were pooled in pairs and paired-end sequenced on one lane of the Illumina HiSeq 2000 at the Stanford Center for Genomics and Personalized Medicine.

Exome-sequencing data analysis. For each exome, raw reads in FASTQ format were aligned to hg19 using the Burrows–Wheeler aligner (BWA, http://bio-bwa.sourceforge.net) to produce a BAM (binary alignment/map) file. For case and each parent, approximately 12 Gb high-quality mappable data were obtained with an average read coverage of 178×, and 90% of bases in the captured region covered more than 49×. SBgenomics BWA-GATK- and Ingenuity Variant Calling platforms version 2.0.20130604 were used to identify potentially pathogenic variants associated with LVNC. An initial variant data set (in variant call format, VCF) was

generated for each sample using the SBgenomics BWA+GATK+Coverage Exome Analysis pipeline. Filtering of variants was carried out on the basis of quality, allele frequency in known populations, pathological potential, genetic analysis, and biological relevance. The initial variant list that contains 2,160,040 variants, affecting 19,706 genes, was filtered for high-confidence variants that met the following quality control: SNPs and indels with overall quality more than 20; and variants with read depth greater than 10. Variants in the top 0.2% of most exonically variable 100 base windows or 1% of most exonically variable genes in the 1000 Genomes project (the database of healthy public genomes; http://www.1000genomes.org/home) were excluded. To obtain more possible pathogenic variants, low-frequency variants with an allele frequency of more than 0.1% in the databases of 1000 Genomes Project, public Complete Genomics genomes (http://www.completegenomics.com/public-data) and NHLBI ESP exomes (http://evs.gs.washington.edu/EVS) were excluded. In addition, suspicious mutations were selected with a focus on suspicious genetic causes that were associated with pathogenic, probably pathogenic, and uncertain significance phenotype. These selected genes have sequence variants associated with (1) non-synonymous mutations including gain of function, loss of function, frame shift, in-frame in-del, start/stop codon change missense that were not tolerated by SIFT or PolyPhen-2; or nucleotide changes in microRNA; or nucleotide changes in likely splice site loss up to 2 bases into intron and structural changes. Finally, 102 variants affecting 108 genes were listed by applying a genetic filtering that selected the genotype occurring in at least two out of the three case samples and not in control samples, as well as by using a biological filtering that kept only variants known to be implicated in LVNC phenotype within 1 hop upstream. Analysed data can be accessed at https://variants.ingenuity.com/Jahanbani2016. Raw data can be accessed as the SRA reference SRP080041.

Genotyping of LVNC patients. The genotype of each family member was determined by isolating genomic DNA from $\sim 5\times10^6$ human fibroblasts or PBMCs, using the DNeasy Blood & Tissue kit (Qiagen) according to the manufacturer's instructions. PCR and direct sequencing was performed as described previously[51]. A detailed list of the primers used is shown in Supplementary Table 11.

shRNA-mediated knockdown. Knockdown of TBX20 was performed using GIPZ Lentiviral Human TBX20 shRNA (V2LHS_286836) and GIPZ Non-silencing Lentiviral shRNA Control (GE Healthcare Dharmacon) according to the manufacturer's protocol. Knockdown efficiency was measured by qRT-PCR.

siRNA-mediated knockdown. Gene knockdown experiments were performed using Lipofectamine RNAiMax (Life Technologies) according to the manufacturer's instructions. Cells were transfected with either scrambled or siRNA against p21 (Life Technologies; siRNA s415; Ambion Silencer Select, 25 nM per well) for 36 h before being subjected to subsequent downstream analysis.

Adenoviral-mediated dominant-negative form of TGF-βRII overexpression. The HEK293T cells were purchased from Thermo Fisher Scientific. The cells were not authenticated or tested for mycoplasma contamination recently. No cell lines used in this study were found in the database of commonly misidentified cell lines that is maintained by ICLAC and NCBI Biosample. For adenoviral vector production, ~80% confluent HEK293T cells were transfected for 48 h with an adenovirus expressing a dominant-negative TGF-β type II receptor[52] or eGFP adenovirus (Vector Biolabs). The collected supernatants were used for the second transduction to concentrate the virus titre. Titres were measured by using the Adeno-X qPCR Titration Kit (Clontech). LVNC iPSC-CMs (1×10^4) were transduced with concentrated viral supernatant containing 2.5×10^4 transducing particles and incubated for 24 h.

Treatment with TGF-β receptor-1 inhibitors. TGF-β receptor-1 inhibitors (SD208, RepSox: Selleckchem) were dissolved in dimethylsulfoxide. An equal concentration of solvent (dimethylsulfoxide) was used as the control. Both iPSC-CMs and ESC-CMs were treated with SD208 or RepSox for 48 h prior to the experiment.

CRISPR–Cas9-mediated genome editing. CRISPR–Cas9-mediated genome editing was performed as previously described[53]. Single-guide DNA oligonucleotides were subcloned into vector PX458 (Addgene), and were delivered into control iPSCs by nucleofection using the P3 Primary Cell 4D-Nucleofector X Kit (Lonza). After 48 h following nucleofection, transfected cells were enriched by fluorescence-activated cell sorting, and established clones were genotyped by PCR and bidirectional direct sequencing.

Transcription activator-like effector nuclease (TALEN)-mediated genome editing. TALEN pair vectors were designed and constructed using the rapid TALEN assembly system as previously described[54]. Five-hundred-base-pair fragments of wild-type *TBX20* exon 7 and adjacent intronic sequences were synthesized as GeneArt String DNA fragments (Life Technologies) to make left and right homologous arms, and cloned into PB-MV1Puro-TK vector (Transposagen), as previously described[55]. Four silent mutations in homologous arms were inserted to create an artificial TTAA site and to avoid re-cleavage of the genomic sequence. Both TALEN pair and targeting vectors were delivered into LVNC iPSCs by nucleofection using P3 Primary Cell 4D-Nucleofector X Kit (Lonza). Afterwards, cells with correct targeting vector integration were selected by puromycin (Life Technologies) and genotyped. To excise the selection cassette, the transient expression of *piggyBac* transposase was performed by nucleofection of excision-only *piggyBac* transposase plasmid, PBx (Transposagen). After negative selection using ganciclovir (Sigma-Aldrich), the established clones were genotyped by PCR and bidirectional direct sequencing.

Statistics and reproducibility. The experiments were not randomized and no statistical method was used to predetermine sample size. No inclusion/exclusion criteria were applied to the animal study. The investigators were not blinded to allocation during experiments and outcome assessment and replicate experiments were performed on the basis of the severity and variability of phenotypes obtained. Data were expressed as mean ± s.e.m. Immunoblots shown are representative of at least two independent experiments. All other experiments are the average of at least two independent assays, and for cell number calculation in immunostaining assays, at least 100 cells per sample were counted for each independent experiments. To confirm the reproducibility, *in vitro* experiments were performed by two independent operators. Statistical analyses were performed using SPSS statistics 21 software (IBM). An unpaired two-tailed Student's *t*-test was used to calculate significant differences between two groups. Multiple comparison correction analysis was performed using ANOVA followed by Tukey's *post hoc* HSD test. A P value of <0.05 was considered statistically significant. For RNA-sequencing, raw P values were adjusted for multiple testing with the Benjamini–Hochberg procedure. Genes with an adjusted P value of 0.05 or less were termed as differentially expressed genes. The investigators were not blinded to allocation during experiments and outcome assessment. Source data are provided in Supplementary Table 12.

Data availability. Primary RNA-seq data sets have been deposited in the Gene Expression Omnibus (GEO) under accession code GSE63161. The Exome-sequencing processed data can be accessed on https://variants.ingenuity.com/Jahanbani2016 and raw data can be accessed as the SRA reference SRP080041. Source data for Figs 1–7 and Supplementary Figs 1–5 have been provided in Supplementary Table 12. All other data supporting the findings of this study are available from the corresponding author on request.

45. Kodo, K. *et al.* GATA6 mutations cause human cardiac outflow tract defects by disrupting semaphorin-plexin signaling. *Proc. Natl Acad. Sci. USA* **106,** 13933–13938 (2009).
46. Stevenson, K. R., Coolon, J. D. & Wittkopp, P. J. Sources of bias in measures of allele-specific expression derived from RNA-sequence data aligned to a single reference genome. *BMC Genomics* **14,** 536 (2013).
47. Abel, E. D. *et al.* Cardiac hypertrophy with preserved contractile function after selective deletion of GLUT4 from the heart. *J. Clin. Invest.* **104,** 1703–1714 (1999).
48. Muzumdar, M. D., Tasic, B., Miyamichi, K., Li, L. & Luo, L. A global double-fluorescent Cre reporter mouse. *Genesis* **45,** 593–605 (2007).
49. Chen, W. P., Liu, Y. H., Ho, Y. J. & Wu, S. M. Pharmacological inhibition of TGFβ receptor improves Nkx2.5 cardiomyoblast-mediated regeneration. *Cardiovasc. Res.* **105,** 44–54 (2015).
50. Hall, B. E. *et al.* Conditional overexpression of TGF-β1 disrupts mouse salivary gland development and function. *Lab. Invest.* **90,** 543–555 (2010).
51. Chang, B. *et al.* 14-3-3ϵ gene variants in a Japanese patient with left ventricular noncompaction and hypoplasia of the corpus callosum. *Gene* **515,** 173–180 (2013).
52. Markell, L. M., Masiuk, K. E., Blazanin, N. & Glick, A. B. Pharmacologic inhibition of ALK5 causes selective induction of terminal differentiation in mouse keratinocytes expressing oncogenic HRAS. *Mol. Cancer Res.* **9,** 746–756 (2011).
53. Ran, F. A. *et al.* Genome engineering using the CRISPR-Cas9 system. *Nat. Protoc.* **8,** 2281–2308 (2013).
54. Ding, Q. *et al.* A TALEN genome-editing system for generating human stem cell-based disease models. *Cell Stem Cell* **12,** 238–251 (2013).
55. Yusa, K. Seamless genome editing in human pluripotent stem cells using custom endonuclease-based gene targeting and the piggyBac transposon. *Nat. Protoc.* **8,** 2061–2078 (2013).

nature cell biology

DOI: 10.1038/ncb3411

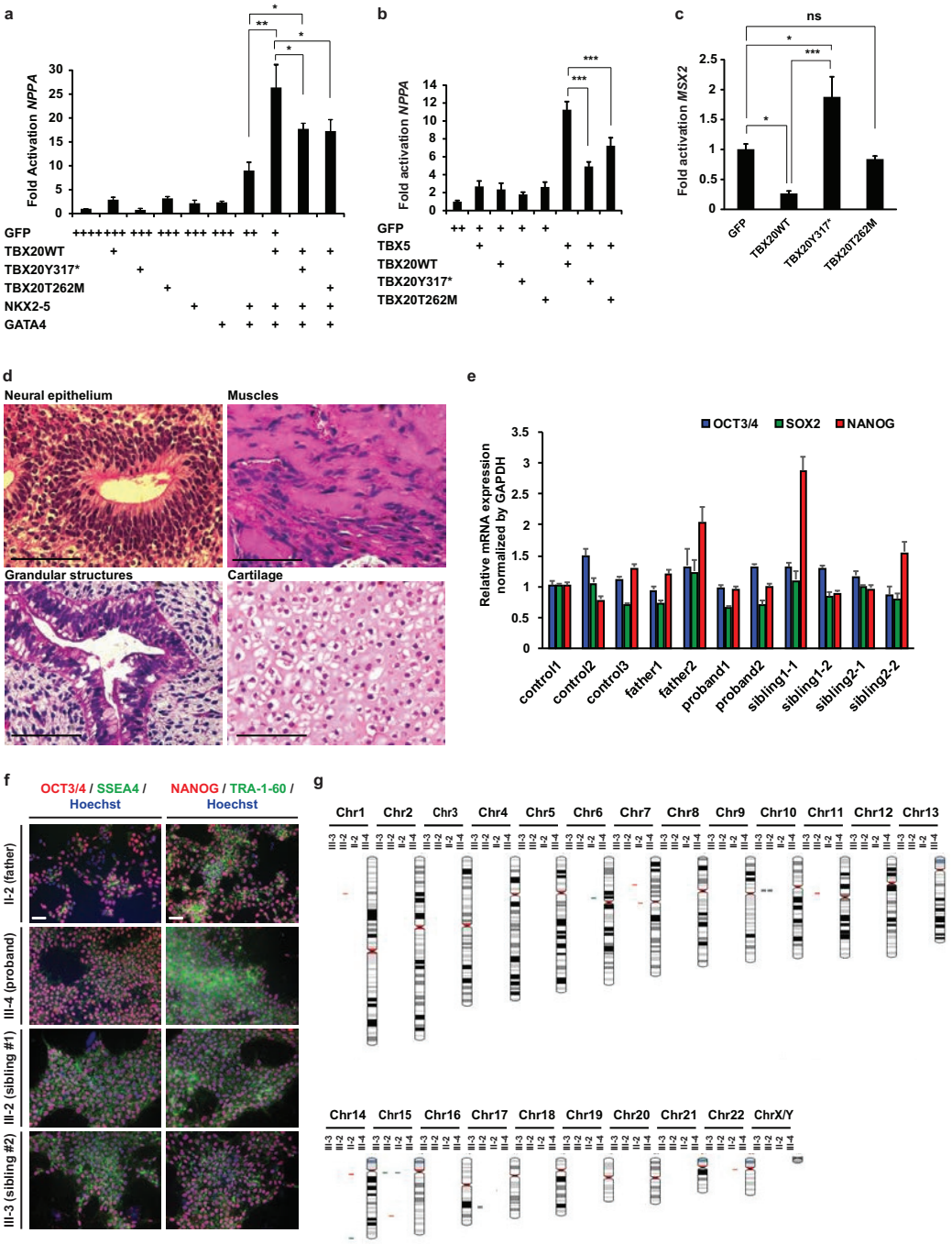

Supplementary Figure 1 Characterization of patient-specific iPSCs. **a-b**, Combined overexpression of cardiac transcription factors and wild-type, Y317*, or T262M mutant TBX20 revealed lack of synergistic activity of mutant TBX20 protein with NKX2-5 and GATA4 (a), or TBX5 (b), on NPPA promoter in luciferase assay using HeLa cells. n=6 independent experiments per each group. **c**, TBX20 Y317* and T262M mutant protein could not repress the MSX2 promoter activity in luciferase assay using HeLa cells. n=6 independent experiments per each group. **d**, iPSCs derived from the family members could form teratomas when injected into a NOD/SCID mouse background, and could differentiate into all three germ layers (ectoderm, endoderm, and mesoderm) as shown by hematoxylin and eosin (HE) staining. **e**, Validation of pluripotent gene expression profile using quantitative real-time PCR (qRT-PCR) in all cell lines n=6 independent experiments per each group. **f**, Immunofluorescence of representative iPSC colony derived from patient-specific fibroblasts or PBMCs staining with markers of pluripotency, including TRA-1-60 (green), OCT3/4 (red), SSEA-4 (green), and NANOG (red). Scale bars, 100 μm. **g**, SNP-based analysis revealed a normal karyotype for all iPSC lines derived from the family members. $*p < 0.05$, $**p < 0.01$, $***p < 0.005$; ns, not significant in one-way ANOVA followed by Tukey post hoc test. The bar graphs show the mean and error bars represent s.e.m. Scale bars, 100 μm. Statistics source data can be found in Supplementary Table 12.

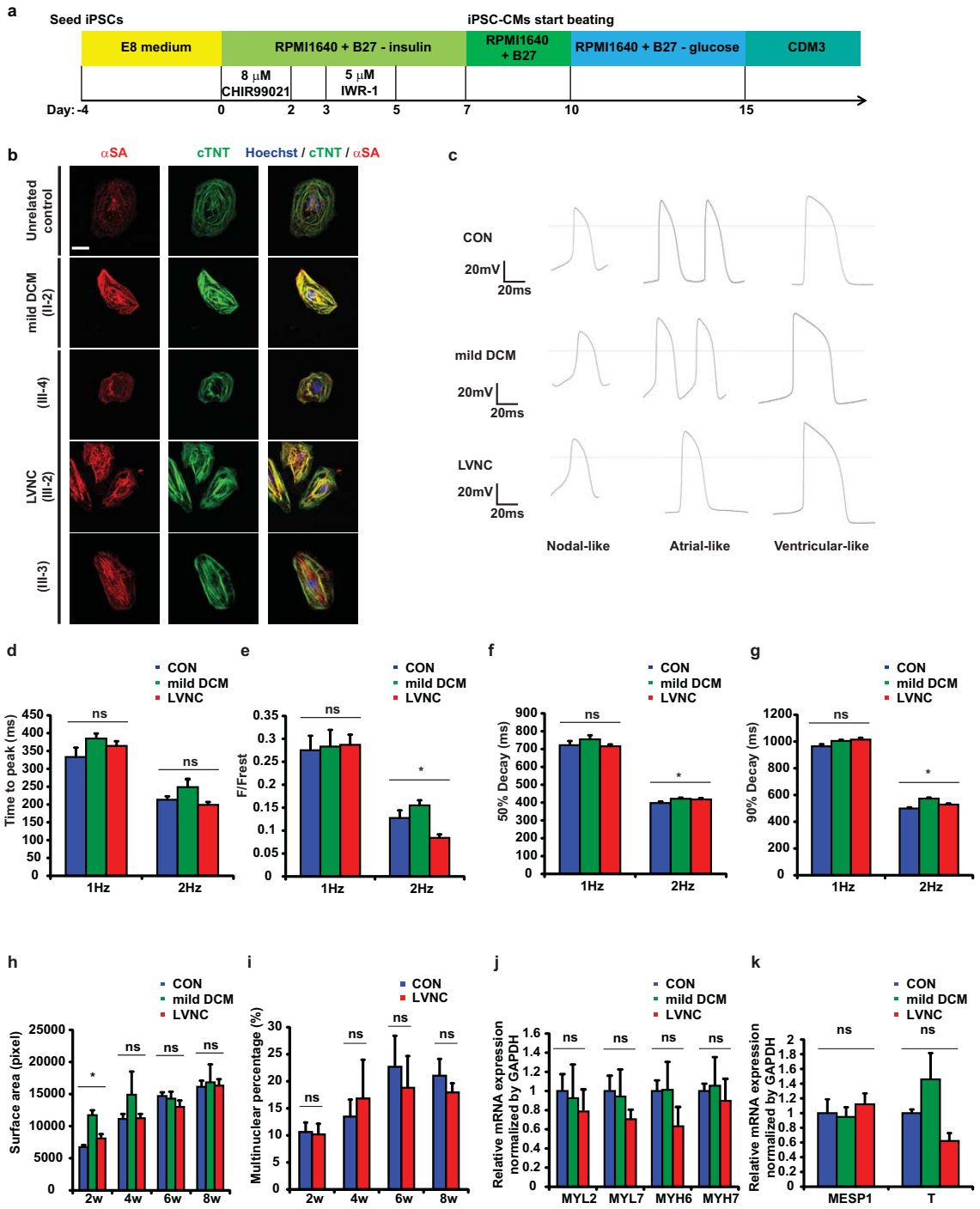

Supplementary Figure 2 Characterization of patient-specific iPSC-CMs. **a**, Schematic of cardiac differentiation protocol. **b**, Representative immunostaining for cardiac troponin T (TNNT2) and alpha-sarcomeric actin (αSA) demonstrating no significant differences in sarcomeric structures between iPSC-CMs from control and family members at 4 weeks after induction of cardiac differentiation. Scale bars, 20 μm. **c,** Spontaneous action potentials in control, mild DCM, and LVNC iPSC-CMs at 4 weeks after induction of cardiac differentiation measured in current-clamp mode. **d-g**, The results of Ca^{2+} imaging study using iPSC-CMs at 4 weeks. Time to peak (d), F/Frest (e), 50% decay (f), and 90% decay (g) were observed between control and patient-specific iPSC-CM lines with 1 Hz or 2 Hz electric stimulation. Data were recorded from n=30 cells (control and mild DCM groups) or n=60 cells (LVNC group). $*p < 0.05$; ns, not significant in one-way ANOVA. **h**, Quantification of cell size for control and patient-specific iPSC-CMs (n=60 cells per group) at 2, 4, 6, and 8 weeks after induction of cardiac differentiation. **i**, Quantification of multinucleation in control and LVNC (III-4) iPSC-CMs at 2, 4, 6, and 8 weeks. n=3 independent experiments per each group. **j**, mRNA expression of sarcomere components in control and patient-specific iPSC-CMs were validated by qRT-PCR at 2 weeks after induction of cardiac differentiation. n=6 independent experiments per each group. **k**, mRNA expression profile of mesodermal transcription factors in differentiating iPSCs were validated by qRT-PCR at 2 days after induction of cardiac differentiation. n=6 independent experiments per each group. CON, unrelated control. $*p < 0.05$; ns, not significant in one-way ANOVA followed by Tukey post hoc test. The bar graphs show the mean and error bars represent s.e.m. Statistics source data can be found in Supplementary Table 12.

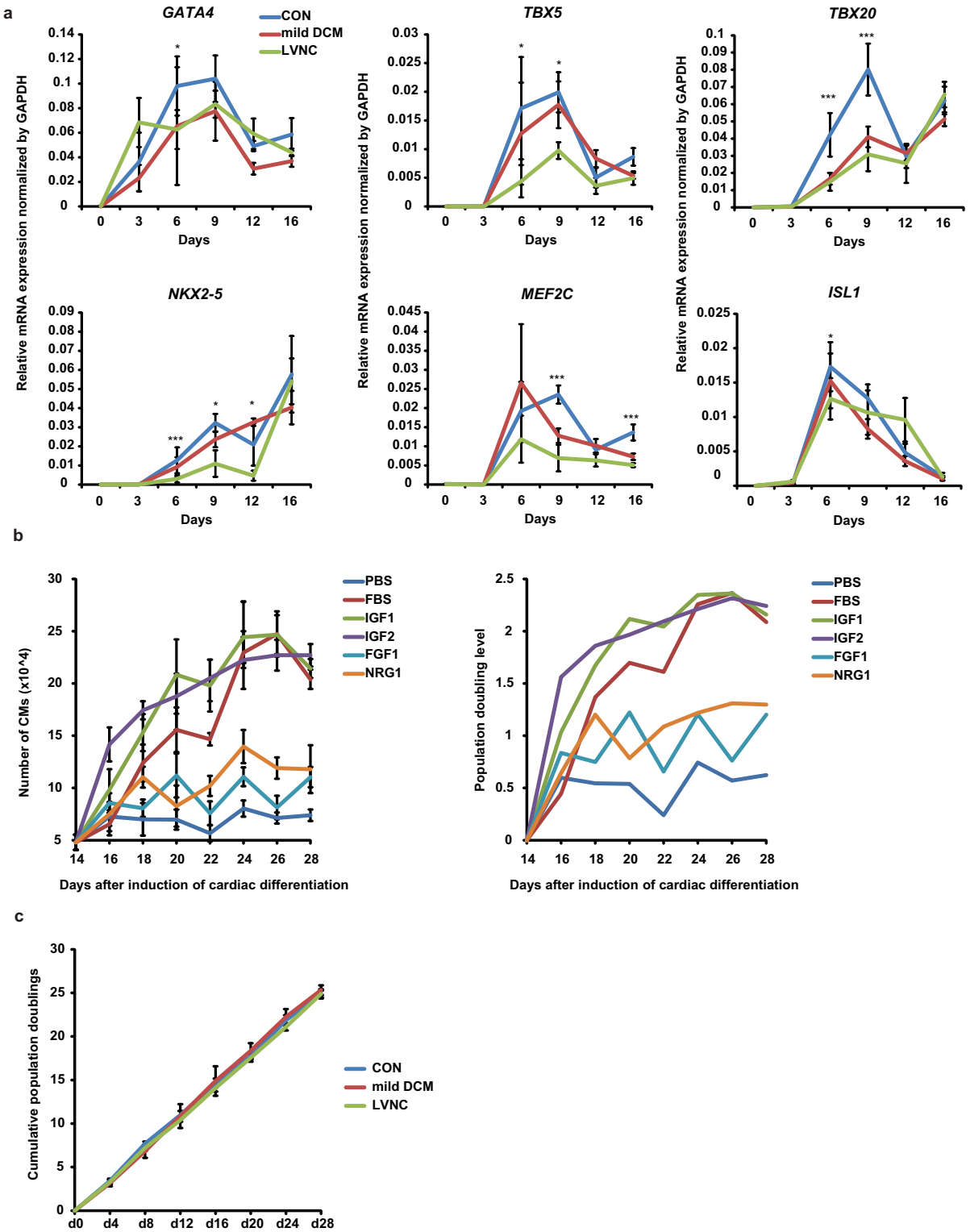

Supplementary Figure 3 Gene expression profile and proliferative potential of differentiating iPSC-CMs. **a**, Relative mRNA expression profile of cardiac transcription factors including *GATA4*, *TBX5*, *NKX2-5*, *MEF2C*, *TBX20*, and *ISL1* from day 0 to day 16 after induction of cardiac differentiation. The LVNC iPSCs showed significant decrease of mRNA expressions of cardiac transcription factors in day 6 and 9. n=6 independent experiments per each group. *$p < 0.05$. ***$p < 0.005$; ns, not significant in one-way ANOVA followed by Tukey post hoc test. **b,** The number (left) and population doubling level (right) of iPSC-CMs with or without serum or growth factors (IGF1, IGF2, FGF1 or NRG1) from day 14 to day 28 after induction of cardiac differentiation. n=6 independent experiments per group. **c**, The measurement of cumulative population doublings showed no significant difference in the growth speed between of control, mild DCM, and LVNC iPSC lines (n=9, 3 and 7 independent experiments for control, mild DCM and LVNC per group respectively). The bar graphs show the mean and error bars represent s.e.m. Statistics source data can be found in Supplementary Table 12.

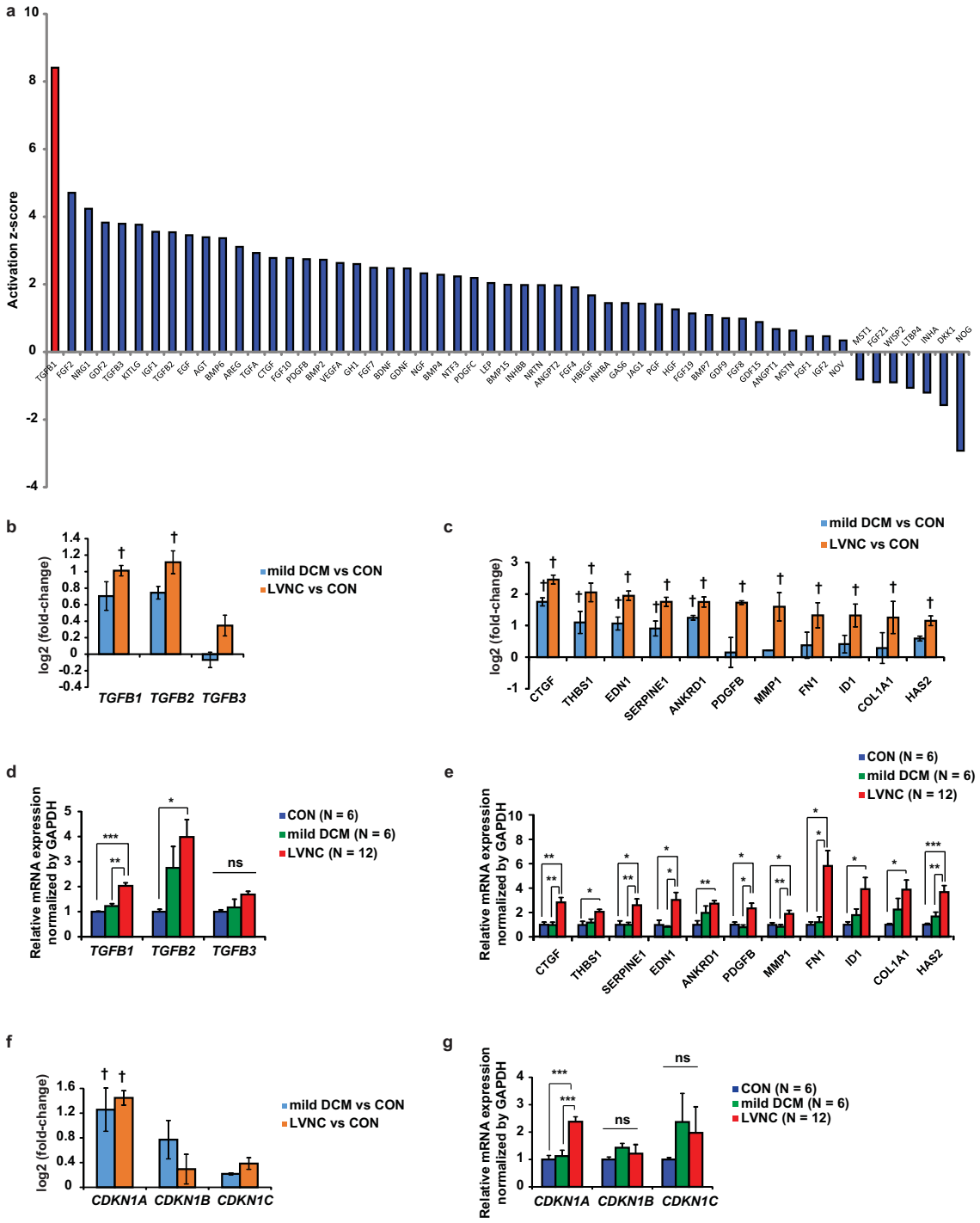

Supplementary Figure 4 Abnormal activation of TGFβ signaling in patient-specific LVNC iPSC-CMs. **a**, Upstream regulator analysis of growth factors comparing LVNC and control iPSC-CMs at 2 weeks. **b**, Significant increase of TGFβ expression in patient-specific iPSC-CMs vs control iPSC-CMs in mRNA-sequencing. Fold-change of mRNA-sequencing data was obtained by FKPM (fragments per kilobase of exon per million) of LVNC (A-III-2, 3, 4; mean of four samples) or mild DCM (A-II-2; mean of two samples) iPSC-CMs per CON (unrelated controls; mean of two samples) iPSC-CMs. **c**, mRNA expression of downstream target genes of TGFβ1 in control and patient-specific iPSC-CMs are validated by mRNA-sequencing at 2 weeks. LVNC iPSC-CMs showed increasing activity of TGFβ signaling compared with control iPSC-CMs (unrelated controls; mean of two samples, mild DCM; mean of two samples, LVNC; mean of four samples). **d-e**, qRT-PCR analysis showed significant increase in TGFβ (d) and downstream target gene (e) mRNA expression in LVNC iPSC-CMs compared to control iPSC-CMs at 2 weeks. **f**, Significant increase of CDKN1A expression in patient-specific iPSC-CMs vs control iPSC-CMs in mRNA-sequencing (unrelated controls; mean of two samples, mild DCM; mean of two samples, LVNC; mean of four samples). **g**, Validation of mRNA expression of cyclin-dependent kinase inhibitors using qRT-PCR. $^{\dagger}q < 0.05$ in Benjamini-Hochberg correction. One-way ANOVA followed by Tukey post hoc test were performed for the validation of qRT-PCR. $^{*}p < 0.05$. $^{**}p < 0.01$. $^{***}p < 0.005$; ns, not significant. The bar graphs show the mean and error bars represent s.e.m. Statistics source data can be found in Supplementary Table 12.

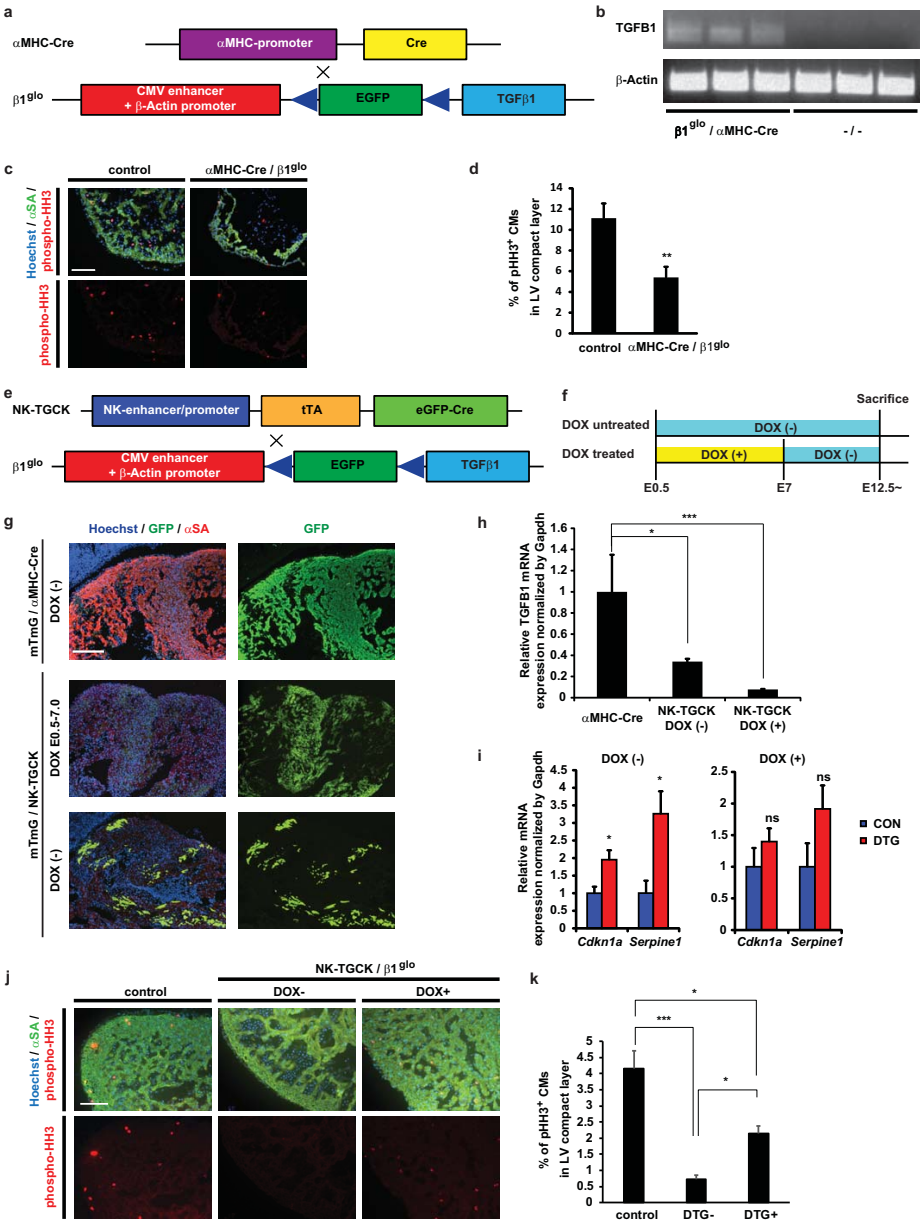

Supplementary Figure 5 Phenotype of cardiomyocyte-specific TGFβ1 overexpression mouse embryos. **a**, The schematic of the $\beta1^{glo}$ and αMHC-Cre transgene. **b**, Activation of TGFB1 transgene in double transgenic ($\beta1^{glo}$/αMHC-Cre) embryos at embryonic day (E) E10.5. Hearts of double transgenic embryos and wild-type littermates (-/-) were corrected and TGFβ1 and Gapdh mRNA expression were validated by RT-PCR. **c**, Immunostaining of nuclear (blue), phosphor-histone H3 (phospho-HH3) (red), and αSA (green) in coronal sections of control and $\beta1^{glo}$/αMHC-Cre double transgenic embryo hearts at E10.5. **d,** Percentage of phospho-histone H3 positive ($pHH3^+$) cardiomyocytes in compact layer of control (n=7 hearts) and $\beta1^{glo}$/αMHC-Cre double transgenic embryo hearts (n=4 hearts) at E10.5. **e,** The schematic of the $\beta1^{glo}$ and NK-TGCK transgene. NK enhancer/promoter-driven eGFP-Cre fusion proteins are expressed without doxycycline (DOX) and tTA proteins inhibit eGFP-Cre expression with existence of DOX. **f**, Schematic of DOX-treatment protocol. **g,** Cre activities of αMHC-Cre and NK-TGCK transgene with or without DOX treatment. αMHC-Cre and NK-TGCK transgenic mice were crossed with mT/mG reporter mice which express cell membrane-localized green fluorescence in Cre recombinase expressing cells. Immunostaining for nuclear (blue), αSA (red), and GFP (green) showed ~90% Cre activity in αMHC-Cre transgenic mouse, ~40% in DOX-untreated NK-TGCK transgenic mouse, and ~25% in DOX-treated NK-TGCK transgenic mouse at E12.5. **h,** mRNA expression of TGFB1 transgene in αMHC-Cre/$\beta1^{glo}$ (n=6 hearts) and NK-TGCK/$\beta1^{glo}$ double transgenic mouse embryos with (n=9 hearts) or without DOX treatment (n=9 hearts) at E10.5. **i**, mRNA expression of TGFB1 downstream target genes including Cdkn1a and Serpine1 in NK-TGCK/$\beta1^{glo}$ double transgenic mouse embryos with (n=5 hearts) or without DOX treatment (n=8 hearts) compared with wild-type littermates (CON; n=5 hearts per group with or without DOX) at E10.5. **j**, Immunostaining of nuclear (blue), phospho-histone H3 (phosphor-HH3) (red), and αSA (green) in coronal sections of wild-type (control) and $\beta1^{glo}$/NE-TGCK double transgenic embryo hearts with (DOX+) or without (DOX-) doxycycline treatment at E12.5. **k,** Percentage of phospho-histone H3 positive ($pHH3^+$) cardiomyocytes in compact layer of control (n=7 hearts) and $\beta1^{glo}$/NE-TGCK double transgenic embryo hearts with (DTG+; n=6 hearts) or without (DTG-; n=7 hearts) doxycycline treatment at E12.5. $*p < 0.05$, $**p < 0.01$, $***p < 0.005$; ns, not significant in unpaired two-tailed *t*-test or one-way ANOVA followed by Tukey post hoc test. The bar graphs show the mean and error bars represent s.e.m. Scale bars, 100 μm. Statistics source data can be found in Supplementary Table 12. Unprocessed original scans of gels are shown in Supplementary Fig. 8.

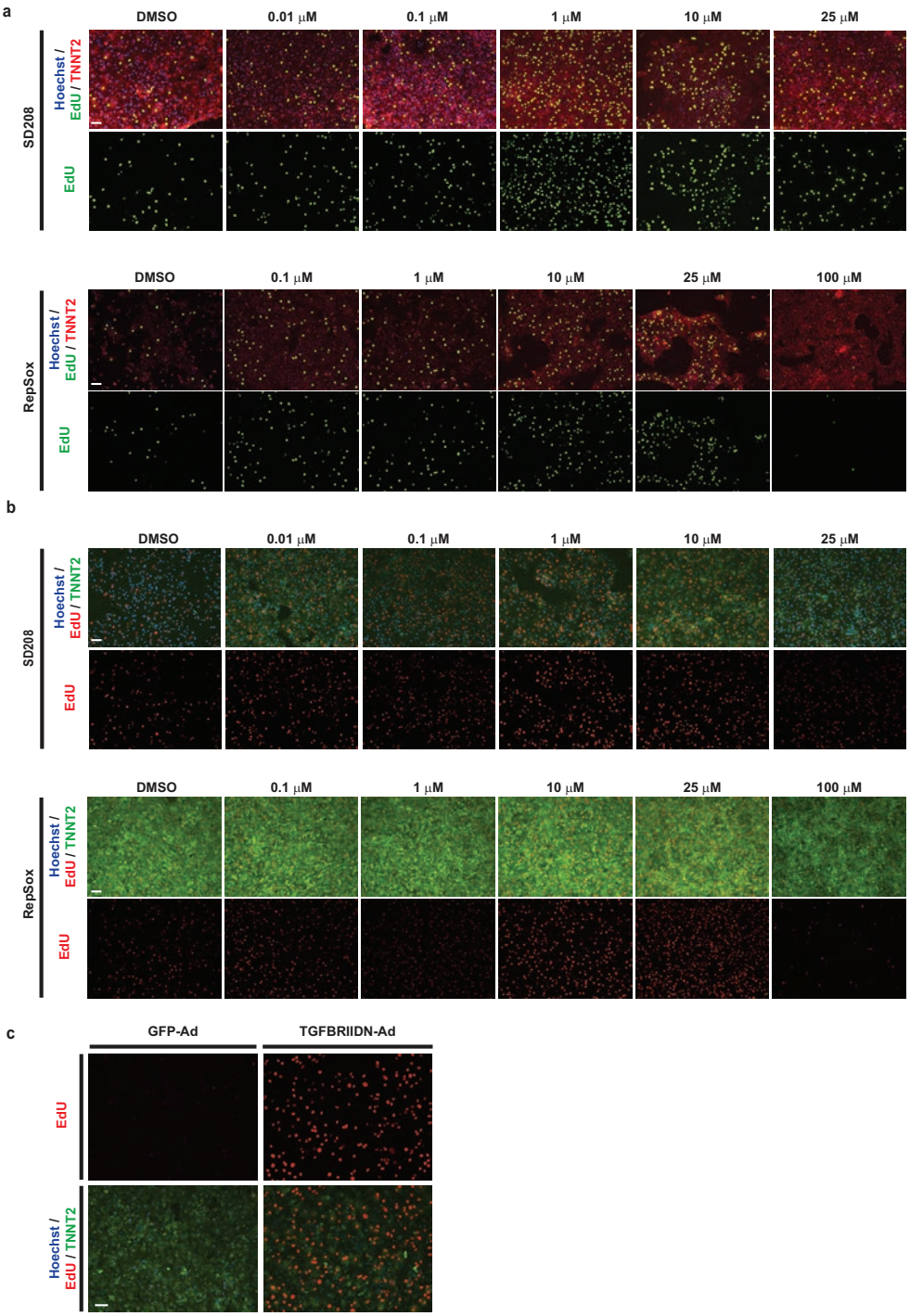

Supplementary Figure 6 Modification of TGFβ signaling rescues proliferation in LVNC iPSC-CMs and TBX20 knockdown ESC-CMs. **a**, Representative immunostaining for nuclear (blue), TNNT2 (red), and EdU (green) in control and LVNC (III-3) iPSC-CMs at 2 weeks after induction of cardiac differentiation with or without treatment of TGFβ receptor-1 inhibitor (SD208 or RepSox) for 2 continuous days. **b**, Representative immunostaining for nuclear (blue), TNNT2 (green), and EdU (red) in scramble and TBX20 knockdown ESC-CMs (TBX20KD ESC-CMs) at 2 weeks after induction of cardiac differentiation with or without treatment of TGFβ receptor-1 inhibitor (SD208 or RepSox) for 2 continuous days. **c**, Representative immunostaining for nuclear (blue), TNNT2 (green), and EdU (red) in LVNC iPSC-CMs at 2 weeks after induction of cardiac differentiation with adenoviral mediated overexpression of GFP (GFP-Ad) or dominant negative form of TGFBRII (TGFBRIIDN-Ad). Scale bars, 100 μm.

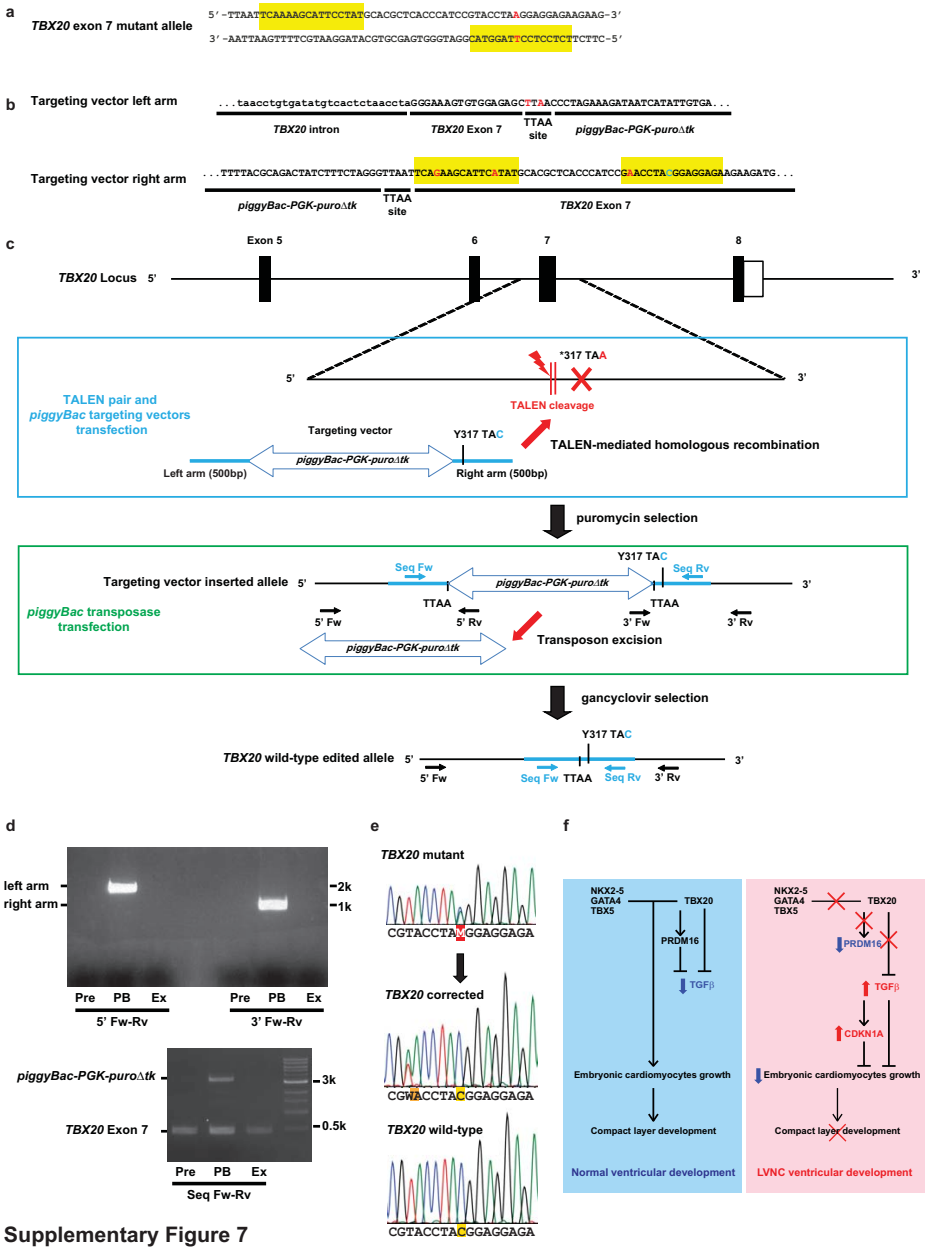

Supplementary Figure 7

Supplementary Figure 7 Generation of TBX20 mutation corrected patient-specific iPSC lines using TALEN. **a,** TALEN recognition sites on *TBX20* exon 7. TALEN pair was designed to bind to the specific sequence of mutant allele including stop-gain mutation site (c.951C>A, red character) using the rapid TALEN assembly system. **b,** Sequence of left and right arms of the targeting vector. To make a targeting vector, 500 bp fragments of left and right arms were designed to share homologies with TBX20 exon 7 carrying wild-type sequence (c.951C, blue character) and flanking introns. TTAA site for *piggyBac* excision was created by introducing silent mutations near the intended modification site (red character in left arm). To avoid re-cleavage of substituted genomic sequence, three silent mutations (red character) were created into the TALEN recognition sites on right arm (yellow box). Both arms were cloned into a vector carrying *piggyBac* transposon with *PGK* promoter *puroΔtk* selection cassette (*PGK-puroΔtk*) to make the targeting vector. **c,** Overview of targeted correction of TBX20 Y317* mutation using TALEN and *piggyBac* transposon system. TALEN-mediated double strand DNA break promotes homologous recombination of the targeting vector into cleaved site, and clones with integrated *PGK-puroΔtk* cassette were selected by puromycin. Subsequently, *piggyBac-PGK-puroΔtk* cassette was excised by transient expression of *piggyBac* transposase. Mutation-corrected lines were obtained after negative selection using ganciclovir treatment. Genotyping primer positions are indicated as Seq Fw, Seq Rv, 5' Fw, 5' Rv, 3' Fw and 3' Rv. **d,** PCR analysis showing transposon removal. Pre, pre-transfection of TALEN pairs and targeting vector; PB, after puromycin selection; Ex, after gancyclovir selection; 5' Fw-Rv, PCR using 5' Fw and 5' Rv primers; 3' Fw-Rv, PCR using 3' Fw and 5' Rv primers; Seq Fw-Rv, PCR using Seq Fw and Seq Rv primers. Unprocessed original scans of gels are shown in Supplementary Fig. 8. **e,** Precise repair of the stop-gain mutation site. Mutation-corrected lines showed the wild-type sequence (c.951C, yellow box) instead of stop-gain mutation (c.951C>M, red box) and possessed the designed synonymous mutation as indicated in the orange box. **f**, Mechanistic schema of the pathology of LVNC caused by TBX20 loss of function mutation. During the myocardium development, Tbx20 interacts with other cardiac transcription factors, including NKX2-5, GATA4, and TBX5, and initiates cardiac chamber-specific gene expression and myocardium growth. On the other hand, TBX20 inhibits activation of TGFβ signaling partially via PRDM16 and promotes embryonic cardiomyocyte proliferation. TBX20 mutation disturbs synergistic regulation of cardiac chamber specification and myocardium growth. Furthermore, failed suppression of TGFβ leads to improper upregulation of CDKN1A and promotes early exit of cardiomyocyte cell cycle. Decreased ventricular cardiomyocyte specification and proliferation leads to failed formation of compact layer of developing myocardium and results in LVNC.

Figure 1e

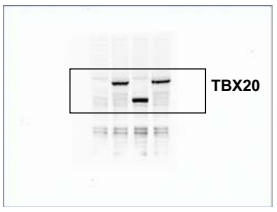

Figure 2c

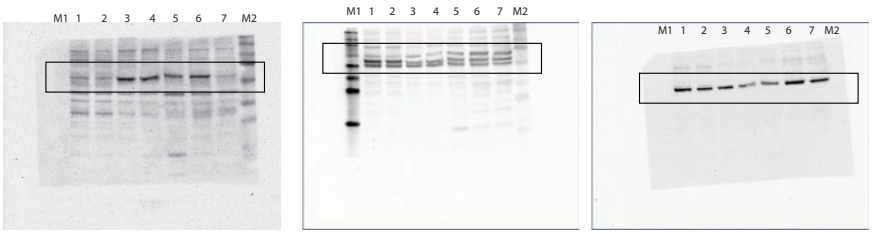

anti-phospho-SMAD2/3 | Biotin-conjugated anti-SMAD2/3 | HRP-conjugated anti-αTubulin

M1: marker (biotinated)
1: control
2: control
3: proband
4: proband
5: sibling#1
6: sibling#2
7: father
M2: marker (unbiotinated)

Figure 2d

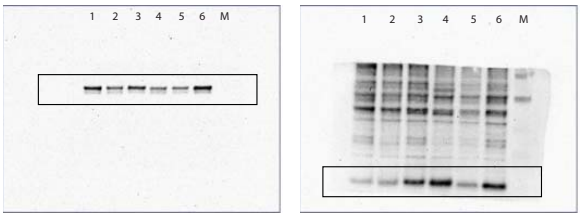

HRP-conjugated anti-αTubulin | anti-CDKN1A

M: marker
1: control
2: father
3: proband
4: proband
5: sibling#1
6: sibling#2

Figure 7d

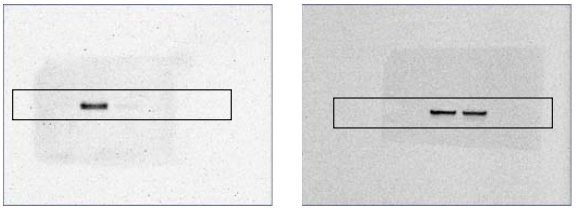

anti-CDKN1A | HRP-conjugated anti-αTubulin

Supplementary Figure 5b

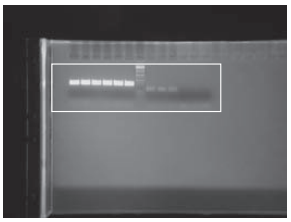

β–Actin TGFB1

Supplementary Figure 7d

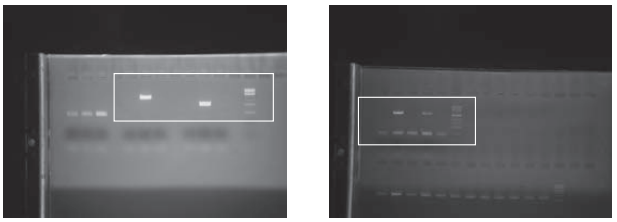

5' Fw-Rv 3' Fw-Rv | Seq Fw-Rv

Supplementary Figure 8 Unprocessed original scans. Uncropped images of scanned western blots and gels shown in the Figures are provided.

Supplementary Table Legends

Supplementary Table 1. Summary of Clinical Phenotype of Recruited Family Members and an Isolated Patient. The clinical information of recruited patients with LVNC are listed.

Supplementary Table 2. The Result of Exome and Direct Sequencing Analysis. a, Rare variants in the proband #1 and the mother. Presence of variant allele in the family members is indicated by "X". **b**, Rare de novo variants in the proband #1.

Supplementary Table 3. Overview on Profiling Assays Performed for Characterization of iPSC-CMs. Experiments for the validation of generated iPSCs in this study are listed.

Supplementary Table 4. Quantification and Detailed Parameters of Current-Clamp Experiments. Detailed parameters used for electrophysiological characterization of 4-weeks patient-specific iPSC-CMs are shown. A-like: Atrial-like myocytes; APA: Action Potential Amplitude; APD50: Action Potential Duration at 50% repolarization; APD70: Action Potential Duration at 70% repolarization; APD90: Action Potential Duration at 90% repolarization; BPM: Beat Per Minute; MDP: Maximal Diastolic Potential; N-like: Nodal-like myocytes; V-like: Ventricular-like myocytes ; Vmax: Upstroke Velocity. Data are shown as mean ± s.e.m.

Supplementary Table 5. IPA Upstream Analysis Data in LVNC vs Control iPSC-CMs. The list of predicted upstream factors analyzed by IPA Upstream Regulator analysis is shown.

Supplementary Table 6. Genotype of Progeny from Heterozygous Crosses of $\beta 1^{glo}$ and αMHC-Cre Transgenic Mice. The Mendelian ratio was observed for embryos collected at E10.5. No double transgenic ($\beta 1^{glo}$/αMHC-Cre) mutants were obtained after E12.5.

Supplementary Table 7. Genotype of Progeny from Heterozygous Crosses of $\beta 1^{glo}$ and NK-TGCK Transgenic Mice with or without DOX Treatment. Without DOX treatment, the Mendelian ratio was observed only at E12.5. On the other hand, the normal distribution of genotype was observed in neonates in DOX-treated group.

Supplementary Table 8. Analogy of Gene Expression Prolife between LVNC iPSC-CMs and Tbx20 Knockout Mouse Heart. Corresponding up- or downregulated gene list (LVNC iPSC-CMs vs. Control iPSC-CMs, Tbx20 knockout mouse heart vs. wild-type mouse heart) is provided.

Supplementary Table 9. Conserved TBX20 Binding Sites between Human and Mouse. TBX20 binding sites predicted by ChIP-sequencing in the well conserved genomic region between human and mouse are listed.

Supplementary Table 10. List of Antibodies Used in this Study. The commercial antibodies used in this study are listed together with their source.

Supplementary Table 11. List of Genotyping Primers. The primer sequences for genotyping the LVNC patients used in this study are listed.

Supplementary Table 12. Statistics Source Data. The source data used for statistical analyses is provided.